ORIGINAL ARTICLE

L. E. Barraza de León · H. Camacho-Montes⊚ **·
Y. Espinosa-Almeyda · J. A. Otero · R. Rodríguez-Ramos ·
J. C. López-Realpozo · F. J. Sabina**

Semi-analytic finite element method applied to short-fiber-reinforced piezoelectric composites

Abstract In this work, a 3D semi-analytical finite element method (SAFEM) is developed to calculate the effective properties of piezoelectric fiber-reinforced composites (PFRC). Here, the calculations are implemented in one-eighth of the unit cell to simplify the method. The prediction of the effective properties for periodic PFRC made of piezoceramic unidirectional fibers (PZT) with square and hexagonal space arrangements in a soft non-piezoelectric matrix (polymer) is reported as a way to validate the 3D approach. The limit case, when short fibers become long ones, allows us to compare with results reported in the literature. For the analysis of effective properties as a function of fiber relative length, two cases are considered: (i) constant volume fraction and (ii) constant fiber radius. The constant volume fraction case is of special interest because according to the Voigt–Reuss–Hill approximation, the effective properties should remain constant. Then, in order to analyze this case, mechanical and electric fields are also shown. The obtained results show a physically congruent behavior. Good coincidences are obtained by comparing with asymptotic homogenization and the representative volume element methods. The 3D SAFEM is also implemented to study the bone piezoelectric behavior with attention to the role of the mineralized phase on the effective d_{333}^* piezoelectric coefficient.

Keywords Piezoelectric short-fiber-reinforced composites · Effective properties · Bone piezoelectricity · Finite element method · Asymptotic homogenization method

1 Introduction

Piezoelectric composite materials (PCM) have been receiving significant attention due to their wide variety of applications as sensors and actuators for measure strain or voltage, vibration control for mechanic structures,

L. E. Barraza de León · H. Camacho-Montes (✉)
Instituto de Ingeniería y Tecnología, Universidad Autónoma de Ciudad Juárez, Av. Del Charro 450 Norte Cd. Juárez,
CP 32310 Chihuahua, México
E-mail: hcamacho@uacj.mx

Y. Espinosa-Almeyda · F. J. Sabina
Instituto de Investigaciones en Matemáticas Aplicadas y en Sistemas, Universidad Nacional Autónoma de México, Apartado
Postal 20-126, 01000 Alcaldía Álvaro Obregón, CDMX, México

J. A. Otero
Tecnológico de Monterrey, Escuela de Ingeniería y Ciencias, CP 52926 Ciudad López Mateos, Estado de México, México

R. Rodríguez-Ramos · J. C. López-Realpozo
Facultad de Matemática y Computación, Universidad de La Habana, San Lázaro y L, Vedado, CP 10400 La Habana, Cuba

noise or flow control, detection of ultrasonic waves, energy harvesters, and so on [1–3]. High piezoelectric performances, large figures of merits, and considerable anisotropy put piezoelectric materials in the applied field of energy harvesting devices [4]. 3D printing of piezoelectric materials is a field that is gaining more relevance in a nonstop manner [5]. The properties, connectivity patterns, and symmetry of the electroceramics composite are explored by Newnham [6]. Also, the fundamental ideas underlying the electroceramics composites are reviewed. Some applications of PCM are reported in Ref. [7]. Besides, the search for lead-free piezoelectric ceramics [8] and the increasing demand for smart materials [9] have also boosted the search for better electroceramics.

From the side of natural materials, the bone piezoelectric behavior has been part of the research activities for a long time [10] and it is still an issue [11]. Bone generation is a topic that covers piezoelectric bioceramics as in Refs. [12–14]. Miara et al. [15] studied piezomaterials for bone regeneration based on a homogenization approach. Bersani et al. [16] presented an overview of recent trends related to mathematical modeling of several enzymatic mechanisms. Also, they illustrated the application to bone and piezoelectricity. More recently, Mohammadkhah et al. [17] developed a review on bone piezoelectricity computer modeling and its key role in bone adaptation and regeneration.

In these searching scenarios, modeling and simulation are expected to play an effective supporting role. In piezoelectric composites, the a priori estimation of the percentage of their phases and constituent parameters allows better control of the effective properties, and hence, a better design of piezoelectric devices. In this sense, several theoretical 2D and 3D models have been developed to estimate the effective piezoelectric coefficients [18–24]. An analytical Hamiltonian-based method to obtain exact solutions for a piezoelectric fiber-reinforced composite (PFRC) cylindrical shells based on the Reissner's shell theory is proposed by Zhou et al. [25]. The piezoelectric effective moduli of PFRC with a micromechanics approach based on the Mori–Tanaka model is investigated by Hasanzadeh et al. [26]. The generalized eigenstrain concept is applied to calculate the effective electroelastic coefficient of PFRC with ring-shaped cross section under antiplane shear coupled with in-plane electric load [27].

Several authors have developed models to describe the structure–properties relationship for 3D representative elements. For example, the three-cell model and the finite element method (FEM) are applied to estimate the effective mechanical properties of a braided piezoelectric ceramic composite [28]. FEM is used to calculate the effective properties of a three-phase magneto-electro-elastic fiber-reinforced composite (FRC) [29]. Multilayered piezoelectric systems are studied using finite element analysis [30]. Zhang et al. developed a 3D approach based on the scaled boundary FEM that can provide an effective elastic coefficient where fibers are treated as truss element, i.e., the fiber is embedded in the matrix element using new nodes in a line intersection with further scaling [31]. This method is efficient for considering a wide orientation distribution of fiber inclusions. A micromechanical model applying finite element with asymptotic volume segmentation for electromechanical properties of PFRC actuator is given by Dubey and Panda [32]. Analytical and numerical approaches to estimate piezoelectric coefficients for macro-reinforced composite are reported in Ref. [33]. All the above-mentioned 3D models are fully based in 3D finite element analysis, anyway, they may have some limitations for considering specific types of inclusions.

Further development in 3D unit cell for effective properties estimations is needed to contribute to the search of electroceramics with improved performance and to better understand of the bone piezoelectric behavior. Herein, a semi-analytical finite element approach (SAFEM) developed in Refs. [34,35] for periodic and elastic FRC with long and unidirectional fibers is extended to consider 3D composite structures. Besides, piezoelectric behavior is added to the model. A combination of the asymptotic homogenization method (AHM) with FEM offers several advantages. From one side, the rigorous mathematical basement of AHM [36,37] warranties the accuracy of the problem statements reducing to zero some consideration that may limit the validity of the model in some situations. From the other side, the FEM is applied at a proceeding step where the problem is stated and almost any kind of unit cell can be considered. For SAFEM, the boundary conditions resulted from a rigorous mathematical procedure rather than a set of hypothetical statements. Then, it is to be expected that the possible limitations must be related to the mesh quality or computer capacities. Therefore, a validation process needs to be developed to investigate the capabilities of the SAFEM approach.

In the present work, a 3D piezoelectric short FRC is studied considering that this kind of structure is of interest [38,39]. Section 2 is devoted to the piezoelectric composite problem statement. Initially, the AHM procedure for 3D problems is presented until the statement of the nine local problems. Then, these local problems are accommodated in such a way to facilitate the FEM implementation, which is developed using the commercial software ANSYS, Inc. (Canonsburg, PA, USA). The effective properties are also accommodated to directly connect them to the ANSYS parameters. In Sect. 3, the effect of fiber length on the effective elastic,

piezoelectric, and dielectric properties of PFRC is analyzed. As a limit case toward a long fiber, comparisons with literature reported coincident and expected values. Further analysis is developed to understand the properties behavior and significant insight into the composite behavior is gained. Finally, due to 3D SAFEM capacity, as a second case of application, the analysis developed by Penta et al. [40] is extended to bone piezoelectric behavior.

2 Fundamental equation of piezoelectric composites: method of solution

A piezoelectric composite material (PCM) is considered which occupies a volume $\Omega \subset \Re^3$ limited by the surface S. The electromechanical coupling equations for this heterogeneous PCM Ω are described by a fundamental partial differential equations system, for a quasi-static approximation. Thus, the stress equilibrium and Gauss's law are assumed considering the absences of body forces and electric charge, as follows:

$$\sigma_{ij,j} = 0, \ D_{i,i} = 0, \ \text{in } \Omega, \tag{1}$$

with $i, j, k, l = 1, 2, 3$ and the linear coupled constitutive equations have the form:

$$\sigma_{ij} = C_{ijkl}\varepsilon_{kl} - e_{kij}E_k, \tag{2}$$
$$D_i = e_{ikl}\varepsilon_{kl} + \kappa_{ik}E_k, \tag{3}$$

where $\varepsilon_{kl} = (u_{k,l} + u_{l,k})/2$ and $E_k = \varphi_{,k}$, and the symmetric properties $C_{ijkl} = C_{klij} = C_{jikl} = C_{ijlk}$, $e_{kij} = e_{kji}, \kappa_{ik} = \kappa_{ki}$, and $\sigma_{ij} = \sigma_{ji}$ are satisfied.

In Eqs. (1)–(3), σ_{ij} and ε_{kl} are the stress and deformation tensors, D_i and E_k are the electric displacements and field vectors, and C_{ijkl}, e_{kij} and κ_{ij} are the stiffness, piezoelectric (relating stress to the electric field), and permittivity tensors, respectively. Also, the summation by repeated Latin indices is assumed and the comma notation indicates the partial derivate relative to the x_j component.

The system [Eq. (1)] together with the conditions on the surface S, boundary of the medium Ω,

$$u_i = \bar{u}_i, \sigma_{ij}n_j = \bar{t}_i, \varphi = \bar{\varphi} \text{ and } D_in_i = \bar{Q}, \text{ on } S \tag{4}$$

define the fundamental linear electromechanical coupling problem of a heterogeneous medium Ω as a function of unknown u_i and φ. Here, the bar symbol over the function represents the prescribed values of displacement u_i, tractions t_i, electric potential φ, and electric charge Q on S.

The three-dimensional heterogeneous piezoelectric structure $\Omega \subset \Re^3$ is defined by a two-phase FRC with doubly periodicity fiber distribution in the coordinate system $\{O\,;\ x_1,\ x_2,\ x_3\}$; see Figs. 1 and 2. The reinforcements (fibers) are short cylinders unidirectionally oriented with equal radii and material properties. They are periodically embedded without overlapping in a homogeneous matrix. Fibers and matrix are transversely isotropic materials; therefore, there are only ten independent material coefficients, 5 elastic, 3 piezoelectric, and 2 dielectric constants. The Ox_3-axis of transverse symmetry of each phase coincides with the fiber reinforcement direction.

Two different periodic unit cells are considered. Figure 1 displays a space square fiber distribution in Ox_1x_2-plane and the unit cell is defined as a cubic matrix with a centered short cylinder (fiber) of radius R and length h, $0 < h < 1$ at the Cartesian system of coordinates $\{O\,;\ y_1,\ y_2,\ y_3\}$. Similarly, Fig. 2 shows a space hexagonal fiber distribution in Ox_1x_2-plane where the unit cell is a parallelepiped with a centered short fiber, as in Fig. 1. The periodic unit cell cross section Y represents a square and hexagonal fiber arrangement, respectively. The regions occupied by the matrix S_1 and fiber S_2 satisfy $Y = S_1 \cup S_2$ and $S_1 \cap S_2 = \varnothing$. The interface between fiber and matrix is defined by $\Gamma = \{z : z = Re^{i\theta}, \ 0 \le \theta \le 2\pi\}$ and it is assumed to behave as a perfect contact, that is, mechanical displacements and tractions, quasi-static electric potential and normal electric displacement remain continuous across the interface Γ, see, for instance, Ref. [41].

2.1 Asymptotic homogenization method: local problems and effective properties

The well-known two-scale asymptotic homogenization method (AHM) reported in Refs. [36,37,42] is applied to find an asymptotic solution for the problem described by Eqs. (1)–(4). Then, displacements u_i and electric potential φ are found posing the Ansatz:

$$u_i(\mathbf{x}) = u_i^{(0)}(\mathbf{x}, \mathbf{y}) + \varepsilon\, u_i^{(1)}(\mathbf{x}, \mathbf{y}) + O(\varepsilon^2), \tag{5}$$
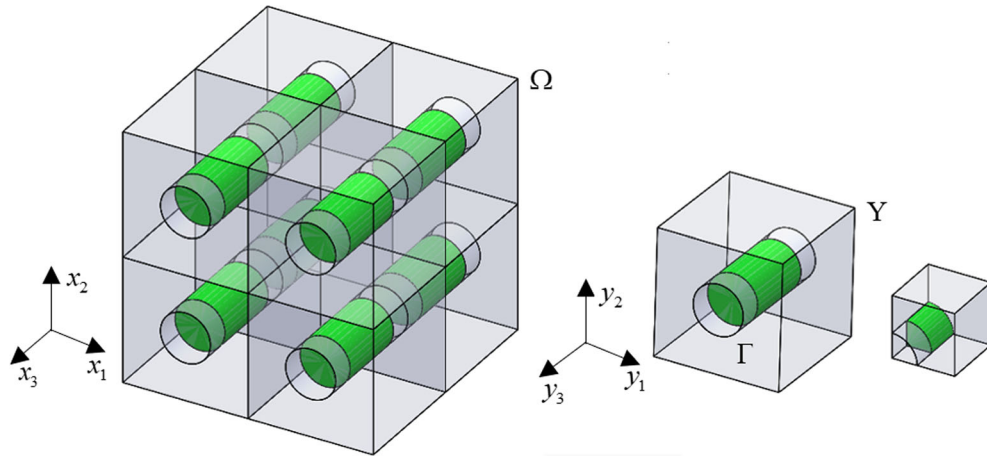
Fig. 1 Periodic structure of composite (left), the unit cell for a space square fiber distribution in Oy_1y_2-plane (middle), and one-eighth of the unit cell (right)
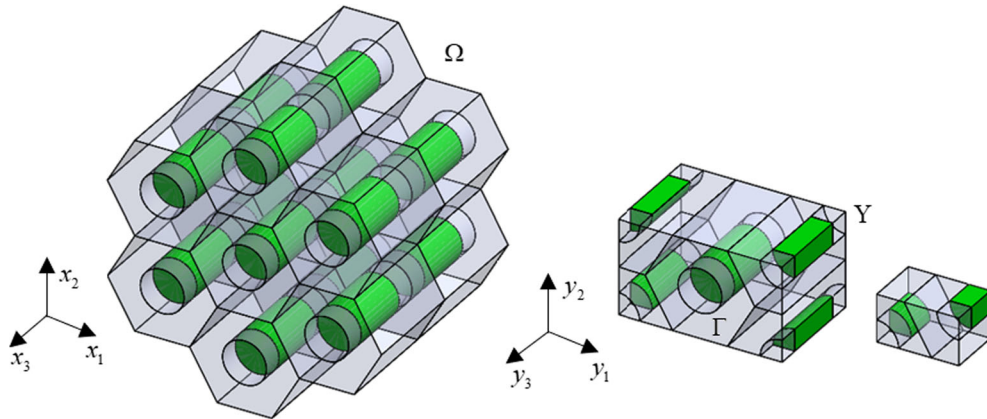

Fig. 2 Periodic structure of composite (left), the unit cell for a space hexagonal fiber distribution in Oy_1y_2-plane (middle), and one-eighth of the unit cell (right)

$$\varphi(\mathbf{x}) = \varphi^{(0)}(\mathbf{x}, \mathbf{y}) + \varepsilon\,\varphi^{(1)}(\mathbf{x}, \mathbf{y}) + O(\varepsilon^2), \tag{6}$$

where the terms $u_i^{(0)}(\mathbf{x}, \mathbf{y}) \equiv u_i^{(0)}(\mathbf{x})$ and $\varphi^{(0)}(\mathbf{x}, \mathbf{y}) \equiv \varphi^{(0)}(\mathbf{x})$ are independent of $\mathbf{y}$. The first-order terms $u_i^{(1)}(\mathbf{x}, \mathbf{y})$ and $\varphi^{(1)}(\mathbf{x}, \mathbf{y})$ are Y-periodic functions of $\mathbf{y}$ which represent a correction of $u_i^{(0)}(\mathbf{x})$ and $\varphi^{(0)}(\mathbf{x})$, respectively. They can be written as:

$$u_i^{(1)}(\mathbf{x}, \mathbf{y}) = {}_{pq}L_i^{(1)}(\mathbf{y})u_{p,q}^{(0)}(\mathbf{x}) + {}_pP_k^{(1)}(\mathbf{y})\,\varphi_{,p}^{(0)}(\mathbf{x}), \tag{7}$$

$$\varphi^{(1)}(\mathbf{x}, \mathbf{y}) = {}_{pq}M^{(1)}(\mathbf{y})u_{p,q}^{(0)}(\mathbf{x}) + {}_pQ^{(1)}(\mathbf{y})\,\varphi_{,p}^{(0)}(\mathbf{x}), \tag{8}$$

where ${}_{pq}L_i^{(1)}(\mathbf{y})$, ${}_{pq}M^{(1)}(\mathbf{y})$, ${}_pP_k^{(1)}(\mathbf{y})$, and ${}_pQ^{(1)}(\mathbf{y})$ are the so-called periodic local functions, which are independent of $\mathbf{x}$ on the cell Y. Herein, the global $\mathbf{x} = (x_1,\ x_2,\ x_3)$ and local $\mathbf{y} = (y_1,\ y_2,\ y_3)$ scales satisfy that $\mathbf{x} = \varepsilon\mathbf{y}$ where $\varepsilon = l/L$ is the ratio between the unit cell length (l) and the characteristic macroscopic dimension of the composite (L). It must be fulfilled that $\varepsilon \ll 1$.

Following the methodology developed in Refs. [41,43], it is possible to obtain two fundamental set of homogenized mathematical problems over the unit cell Y, denoted as ${}_{pq}\mathcal{L}$ and ${}_p\mathcal{I}$ with $p, q = 1,\ 2,\ 3$, and the corresponding effective properties, defined below.

Hence, the mathematical statement of the local problems over Y can be stated as:
${}_{pq}\mathcal{L}$ problems

$$\left(C_{ijpq} + C_{ijkl}\,{}_{pq}L_{k,l} + e_{lij}\,{}_{pq}M_{,l}\right)_{,j} = 0, \quad \left(e_{ipq} + e_{ikl}\,{}_{pq}L_{k,l} - \kappa_{il}\,{}_{pq}M_{,l}\right)_{,i} = 0, \quad \text{on Y} \tag{9}$$

Table 1 Local problems and associated effective properties

$_{11}\mathcal{L}$	$_{22}\mathcal{L}$	$_{33}\mathcal{L}$	$_{23}\mathcal{L}$	$_{13}\mathcal{L}$	$_{12}\mathcal{L}$	$_{1}\mathcal{I}$	$_{2}\mathcal{I}$	$_{3}\mathcal{I}$
C^*_{1111}	C^*_{2211}	C^*_{3311}	0	0	0	0	0	e^*_{311}
C^*_{1122}	C^*_{2222}	C^*_{3322}	0	0	0	0	0	e^*_{322}
C^*_{1133}	C^*_{2233}	C^*_{3333}	0	0	0	0	0	e^*_{333}
0	0	0	C^*_{2323}	0	0	0	e^*_{223}	0
0	0	0	0	C^*_{1313}	0	e^*_{113}	0	0
0	0	0	0	0	C^*_{1212}	0	0	0
0	0	0	0	e^*_{113}	0	κ^*_{11}	0	0
0	0	0	e^*_{223}	0	0	0	κ^*_{22}	0
e^*_{311}	e^*_{322}	e^*_{333}	0	0	0	0	0	κ^*_{33}

$$_{pq}L^{(1)}_k = \,_{pq}L^{(2)}_k, \,_{pq}M^{(1)} = \,_{pq}M^{(2)}, \quad \text{on } \Gamma \tag{10}$$

$$\left[C^{(1)}_{ijpq} + C^{(1)}_{ijkl} \,_{pq}L^{(1)}_{k,l} + e^{(1)}_{lij} \,_{pq}M^{(1)}_{,l} \right] n^{(1)}_j \Big|_\Gamma = -\left[C^{(2)}_{ijpq} + C^{(2)}_{ijkl} \,_{pq}L^{(2)}_{k,l} + e^{(2)}_{lij} \,_{pq}M^{(2)}_{,l} \right] n^{(2)}_j \Big|_\Gamma,$$

$$\left[e^{(1)}_{ipq} + e^{(1)}_{ikl} \,_{pq}L^{(1)}_{k,l} - \kappa^{(1)}_{il} \,_{pq}M^{(1)}_{,l} \right] n^{(1)}_i \Big|_\Gamma = -\left[e^{(2)}_{ipq} + e^{(2)}_{ikl} \,_{pq}L^{(2)}_{k,l} - \kappa^{(2)}_{il} \,_{pq}M^{(2)}_{,l} \right] n^{(2)}_i \Big|_\Gamma,$$

$$\text{on } \Gamma \tag{11}$$

$$\langle_{pq}L_k\rangle = 0, \langle_{pq}M\rangle = 0, \tag{12}$$

where $_{pq}L_k$ (displacements) and $_{pq}M$ (electric potential) are local functions that need found in Y.

$_p\mathcal{I}$ problems

$$\left(e_{pij} + C_{ijkl} \,_pP_{k,l} + e_{lij} \,_pQ_{,l} \right)_{,j} = 0, \quad \left(-\kappa_{ip} + e_{ikl} \,_pP_{k,l} - \kappa_{il} \,_pQ_{,l} \right)_{,i} = 0, \quad \text{on Y} \tag{13}$$

$$_pP^{(1)}_k = \,_pP^{(2)}_k, \,_pQ^{(1)} = \,_pQ^{(2)}, \text{ on } \Gamma \tag{14}$$

$$\left[e^{(1)}_{pij} + C^{(1)}_{ijkl} \,_pP^{(1)}_{,l} + e^{(1)}_{lij} \,_pQ^{(1)}_{,l} \right] n^{(1)}_j \Big|_\Gamma = -\left[e^{(2)}_{pij} + C^{(2)}_{ijkl} \,_pP^{(2)}_{,l} + e^{(2)}_{lij} \,_pQ^{(2)}_{,l} \right] n^{(2)}_j \Big|_\Gamma,$$

$$\left[-\kappa^{(1)}_{ip} + e^{(1)}_{ikl} \,_pP^{(1)}_{,l} - \kappa^{(1)}_{il} \,_pQ^{(1)}_{,l} \right] n^{(1)}_i \Big|_\Gamma = -\left[-\kappa^{(2)}_{ip} + e^{(2)}_{ikl} \,_pP^{(2)}_{,l} - \kappa^{(2)}_{il} \,_pQ^{(2)}_{,l} \right] n^{(2)}_i \Big|_\Gamma,$$

$$\text{on } \Gamma \tag{15}$$

$$\langle_pP_k\rangle = 0, \langle_pQ\rangle = 0, \tag{16}$$

where $_pP_k$ (displacements) and $_pQ$ (electric potential) are local functions that need to be found in Y.

In both $_{pq}\mathcal{L}$ and $_p\mathcal{I}$ problems, $\langle f \rangle = |Y|^{-1} \int_Y f(y)\, dY$ represents the volume average per unit length in Y and the comma notation indicates the partial derivate relative to the y_j component. Also, all local functions and coefficients are dependent of the local variable **y**. Once the above local problem solutions are found, the effective coefficients can be calculated following the formulae:

Associated with the local problems $_{pq}\mathcal{L}$

$$C^*_{ijpq} = \langle C_{ijpq} + C_{ijkl} \,_{pq}L_{k,l} + e_{lij} \,_{pq}M_{,l} \rangle, e^*_{ipq} = \langle e_{ipq} + e_{ikl} \,_{pq}L_{k,l} - \kappa_{il} \,_{pq}M_{,l} \rangle, \tag{17}$$

Associated with the local problems $_p\mathcal{I}$

$$e^*_{pij} = \langle e_{pij} + C_{ijkl} \,_pP_{k,l} + e_{lij} \,_pQ_{,l} \rangle, \kappa^*_{ip} = \langle \kappa_{ip} - e_{ikl} \,_pP_{k,l} + \kappa_{lk} \,_pQ_{,l} \rangle. \tag{18}$$

Notice that effective coefficients [Eqs. (17) and (18)] depend on the local functions linked to the corresponding local problem. These local functions are calculated using the semi-analytical approach describes in the following sections. More details about AHM procedure can be found in Refs. [44,45]. In Table 1 is illustrated the relation between effective properties and local problems.

Table 2 Local problems and transformation conditions

Local problem	Transformation conditions
$_{pq}\mathcal{L}$	$_{pq}L_k = {_{pq}}\hat{L}_k - y_p\delta_{kq}, \; {_{pq}}M = {_{pq}}\hat{M}$
$_p\mathcal{I}$	$_pP_k = {_p}\hat{P}_k, \; {_p}Q = {_p}\hat{Q} - y_p$

2.2 Semi-analytical approach (SAFEM)

In this work, the semi-analytical solution of the homogenized local problems $_{pq}\mathcal{L}$ [Eqs. (9)–(12)] and $_p\mathcal{I}$ [Eqs. (13)–(16)] and the associate effective coefficients [Eqs. (17)–(18)] are found using FEM implemented by ANSYS, Inc. (Canonsburg, PA, USA). First, the homogenized local problems are transformed into equivalent ones in one-eighth of the cell Y (Figs. 1 and 2), and then their solutions are implemented using ANSYS. The local problem transformations are possible considering that periodic unit cell and/or constituent material coefficients satisfy some spatial symmetry conditions, like in the present work, i.e., the unit cell is divided by three perpendicular mirrors. Second, the piezoelectric effective moduli are calculated. This solution procedure is similar to the methodology developed in Refs. [34,35] for a 2D problem, in which the semi-analytical solution of local boundary problems is calculated by FEM through minimum potential energy principle for elastic composites. Herein, SAFEM is expanded to consider piezoelectric behaviors in 3D problems.

Local problems in an eighth of Y *and boundary conditions*

The boundary value problems over one-eighth of the unit cell Y concerning to the homogenized local problems $_{pq}\mathcal{L}$ [Eqs. (9)–(12)] and $_p\mathcal{I}$ [Eqs. (13)–(16)] take place assuming that constituent properties are even functions with respect to the y_i and replacing the local function transformation conditions given in Table 2 into Eqs. (9) and (13), see Refs. [34]. The "caret" symbol over the local functions represents the equivalent pseudo-displacements and pseudo-electric potential local function in one-eighth of periodic unit cell Y.

Therefore, the boundary value problems over one-eighth of Y are defined as follows:

$_{pq}\mathcal{L}$ problems

$$_{pq}\hat{\sigma}_{ij,j} = 0, \quad {_{pq}}\hat{D}_{i,i} = 0, \text{ on } S_\alpha, \tag{19}$$

where $_{pq}\hat{\sigma}_{ij} = C_{ijkl}\, {_{pq}}\hat{L}_{k,l} + e_{lij}\, {_{pq}}\hat{M}_{,l}$ and $_{pq}\hat{D}_i = e_{ikl}\, {_{pq}}\hat{L}_{k,l} - \kappa_{il}\, {_{pq}}\hat{M}_{,l}$.

$_p\mathcal{I}$ problems

$$_p\hat{\sigma}_{ij,j} = 0, \quad {_p}\hat{D}_{i,i} = 0, \text{ on } S_\alpha, \tag{20}$$

where $_p\hat{\sigma}_{ij} = C_{ijkl}\, {_p}\hat{P}_{k,l} + e_{lij}\, {_p}\hat{Q}_{,l}$ and $_p\hat{D}_i = e_{ikl}\, {_p}\hat{P}_{k,l} - \kappa_{il}\, {_p}\hat{Q}_{,l}$.

The $_{pq}\mathcal{L}$ [Eq. (19)] and $_p\mathcal{I}$ [Eq. (20)] problems are subject to boundary conditions, which are summarized in Table 3. Here, $d_h = \{0, \; l_h\}$ where l_h is the periodic unit cell length in the y_h-direction. Also, the boundaries on one-eighth of Y are defined as

$$\{y_1 = d_1, \; y_2, y_3\} \equiv \left\{(y_1, \; y_2, y_3) \in \mathbb{R}^3 \middle| y_1 = \{0, l_1\}, \; 0 \le y_2 \le l_2, \; 0 \le y_3 \le l_3\right\},$$

$$\{y_1, \; y_2 = d_2, y_3\} \equiv \left\{(y_1, \; y_2, y_3) \in \mathbb{R}^3 \middle| 0 \le y_1 \le l_2, \; y_2 = \{0, l_2\}, \; 0 \le y_3 \le l_3\right\}, \text{ and}$$

$$\{y_1, \; y_2, y_3 = d_3\} \equiv \left\{(y_1, \; y_2, y_3) \in \mathbb{R}^3 \middle| 0 \le y_1 \le l_2, \; 0 \le y_2 \le l_2, \; y_3 = \{0, l_3\}\right\}.$$

Thus, the corresponding piezoelectric effective moduli over one-eighth of Y [Eqs. (17) and (18)] are rewritten as:

Associated with the $_{pq}\mathcal{L}$ problem,

$$C^*_{ijpq} = 8\left\langle {_{pq}}\hat{\sigma}_{ij}\right\rangle, e^*_{ipq} = 8\left\langle {_{pq}}\hat{D}_i\right\rangle. \tag{21}$$

Associated with the $_p\mathcal{I}$ problem,

$$e^*_{pij} = 8\left\langle {_p}\hat{\sigma}_{ij}\right\rangle, \kappa^*_{ip} = 8\left\langle {_p}\hat{D}_i\right\rangle. \tag{22}$$

Table 3 Local problems and boundary conditions

Local problem	Boundary conditions	Boundary regions
$_{11}\mathcal{L}$	$_{11}\hat{\sigma}_{12}=0,\ _{11}\hat{\sigma}_{13}=0,\ _{11}\hat{L}_1=d_1,\ _{11}\hat{D}_1=0,$ $_{11}\hat{\sigma}_{21}=0,\ _{11}\hat{\sigma}_{23}=0,\ _{11}\hat{L}_2=0,\ _{11}\hat{D}_2=0,$ $_{11}\hat{\sigma}_{31}=0,\ _{11}\hat{\sigma}_{32}=0,\ _{11}\hat{L}_3=0,\ _{11}\hat{M}=0,$	in $\{y_1=d_h,\ y_2,\ y_3\}$ in $\{y_1,\ y_2=d_h,\ y_3\}$ in $\{y_1,\ y_2,\ y_3=d_h\}$
$_{22}\mathcal{L}$	$_{22}\hat{\sigma}_{12}=0,\ _{22}\hat{\sigma}_{13}=0,\ _{22}\hat{L}_1=0,\ _{22}\hat{D}_1=0,$ $_{22}\hat{\sigma}_{21}=0,\ _{22}\hat{\sigma}_{23}=0,\ _{22}\hat{L}_2=y_2,\ _{22}\hat{D}_2=0,$ $_{22}\hat{\sigma}_{31}=0,\ _{22}\hat{\sigma}_{32}=0,\ _{22}\hat{L}_3=0,\ _{22}\hat{M}=0,$	in $\{y_1=d_h,\ y_2,\ y_3\}$ in $\{y_1,\ y_2=d_h,\ y_3\}$ in $\{y_1,\ y_2,\ y_3=d_h\}$
$_{33}\mathcal{L}$	$_{33}\hat{\sigma}_{12}=0,\ _{33}\hat{\sigma}_{13}=0,\ _{33}\hat{L}_1=0,\ _{33}\hat{D}_1=0,$ $_{33}\hat{\sigma}_{21}=0,\ _{33}\hat{\sigma}_{23}=0,\ _{33}\hat{L}_2=0,\ _{33}\hat{D}_2=0,$ $_{33}\hat{\sigma}_{31}=0,\ _{33}\hat{\sigma}_{32}=0,\ _{33}\hat{L}_3=y_3,\ _{33}\hat{M}=0,$	in $\{y_1=d_h,\ y_2,\ y_3\}$ in $\{y_1,\ y_2=d_h,\ y_3\}$ in $\{y_1,\ y_2,\ y_3=d_h\}$
$_{13}\mathcal{L}$	$_{13}\hat{\sigma}_{11}=0,\ _{13}\hat{L}_2=0,\ _{13}\hat{L}_3=y_1,\ _{13}\hat{M}=0,$ $_{13}\hat{\sigma}_{21}=0,\ _{13}\hat{\sigma}_{23}=0,\ _{13}\hat{L}_2=0,\ _{13}\hat{D}_2=0,$ $_{13}\hat{\sigma}_{33}=0,\ _{13}\hat{L}_1=0,\ _{13}\hat{L}_2=0,\ _{13}\hat{D}_3=0,$	in $\{y_1=d_h,\ y_2,\ y_3\}$ in $\{y_1,\ y_2=d_h,\ y_3\}$ in $\{y_1,\ y_2,\ y_3=d_h\}$
$_{23}\mathcal{L}$	$_{23}\hat{\sigma}_{12}=0,\ _{23}\hat{\sigma}_{13}=0,\ _{23}\hat{L}_1=0,\ _{23}\hat{D}_1=0,$ $_{23}\hat{\sigma}_{22}=0,\ _{23}\hat{L}_1=0,\ _{23}\hat{L}_3=y_2,\ _{23}\hat{M}=0,$ $_{23}\hat{\sigma}_{33}=0,\ _{23}\hat{L}_1=0,\ _{23}\hat{L}_2=0,\ _{23}\hat{D}_3=0,$	in $\{y_1=d_h,\ y_2,\ y_3\}$ in $\{y_1,\ y_2=d_h,\ y_3\}$ in $\{y_1,\ y_2,\ y_3=d_h\}$
$_{12}\mathcal{L}$	$_{12}\hat{\sigma}_{11}=0,\ _{12}\hat{L}_2=y_1,\ _{12}\hat{L}_3=0,\ _{12}\hat{M}=0,$ $_{12}\hat{\sigma}_{22}=0,\ _{12}\hat{L}_1=0,\ _{12}\hat{L}_3=0,\ _{12}\hat{M}=0,$ $_{12}\hat{\sigma}_{31}=0,\ _{12}\hat{\sigma}_{32}=0,\ _{12}\hat{L}_3=0,\ _{12}\hat{M}=0,$	in $\{y_1=d_h,\ y_2,\ y_3\}$ in $\{y_1,\ y_2=d_h,\ y_3\}$ in $\{y_1,\ y_2,\ y_3=d_h\}$
$_{1}\mathcal{I}$	$_{1}\hat{\sigma}_{11}=0,\ _{1}\hat{P}_2=0,\ _{1}\hat{P}_3=0,\ _{1}\hat{Q}=y_1,$ $_{1}\hat{\sigma}_{21}=0,\ _{1}\hat{\sigma}_{23}=0,\ _{1}\hat{P}_2=0,\ _{1}\hat{D}_2=0,$ $_{1}\hat{\sigma}_{33}=0,\ _{1}\hat{P}_1=0,\ _{1}\hat{P}_2=0,\ _{1}\hat{D}_3=0,$	in $\{y_1=d_h,\ y_2,\ y_3\}$ in $\{y_1,\ y_2=d_h,\ y_3\}$ in $\{y_1,\ y_2,\ y_3=d_h\}$
$_{2}\mathcal{I}$	$_{2}\hat{\sigma}_{12}=0,\ _{2}\hat{\sigma}_{13}=0,\ _{2}\hat{P}_1=0,\ _{2}\hat{D}_1=0,$ $_{2}\hat{\sigma}_{22}=0,\ _{2}\hat{P}_1=0,\ _{2}\hat{P}_3=0,\ _{2}\hat{Q}=y_2,$ $_{2}\hat{\sigma}_{33}=0,\ _{2}\hat{P}_1=0,\ _{2}\hat{P}_2=0,\ _{2}\hat{D}_3=0,$	in $\{y_1=d_h,\ y_2,\ y_3\}$ in $\{y_1,\ y_2=d_h,\ y_3\}$ in $\{y_1,\ y_2,\ y_3=d_h\}$
$_{3}\mathcal{I}$	$_{3}\hat{\sigma}_{12}=0,\ _{3}\hat{\sigma}_{13}=0,\ _{3}\hat{P}_1=0,\ _{3}\hat{D}_1=0,$ $_{3}\hat{\sigma}_{21}=0,\ _{3}\hat{\sigma}_{23}=0,\ _{3}\hat{P}_2=0,\ _{3}\hat{D}_2=0,$ $_{3}\hat{\sigma}_{31}=0,\ _{3}\hat{\sigma}_{32}=0,\ _{3}\hat{P}_3=0,\ _{3}\hat{Q}=y_3,$	in $\{y_1=d_h,\ y_2,\ y_3\}$ in $\{y_1,\ y_2=d_h,\ y_3\}$ in $\{y_1,\ y_2,\ y_3=d_h\}$

According to the effective coefficient formulations, the pseudo-local functions (pseudo-displacement and pseudo-electrical potential) need to be found for each local boundary problem over one-eighth of Y. The whole set of piezoelectric effective moduli is determined through the solutions of all local problems.

ANSYS numerical implementation

The numerical solution of the $_{pq}\mathcal{L}$ and $_{p}\mathcal{I}$ local problems [Eqs. (19) and (20)] subject to boundaries conditions (Table 3) is solved by finite element method implemented via ANSYS. The ANSYS software (Canonsburg, PA, USA) is considered because it is highly trustable and efficient. The piezoelectric behavior can be described with the element "solid98" of the ANSYS library. This is a 3D tetrahedral element with 10 nodes. The square unit cell of Fig. 1 is meshed as shown in Fig. 3 for a set of different relative fiber lengths. Analogously, the hexagonal unit cell of Fig. 2 is also meshed, but it is not shown here for simplicity.

For the numerical implementation of the and $_{p}\mathcal{I}$ local problems [Eqs. (19) and (20)] under the boundaries conditions of Table 3, the ANSYS coordinate system is taken as shown in Fig. 1. ANSYS mechanical displacements and electrical potential are considered as $_{pq}\hat{L}_k$ and $_{pq}\hat{M}$ $\left(_{p}\hat{P}_k \text{ and } _{p}\hat{Q}\right)$ for the $_{pq}\mathcal{L}\left(_{p}\mathcal{I}\right)$ problems. The $_{F}\hat{\sigma}_{ij}$ with $ij=11,\ 22,\ 33$ corresponds to ANSYS X, Y and Z stress components, as well as $ij=12,\ 13,\ 23$ to the shear stresses XY, YZ and XZ. The ANSYS electrical displacement is $_{F}\hat{D}_i$ with $i=1,\ 2,\ 3$. The F pre-index (pq and p) is used to identify the corresponding $_{pq}\mathcal{L}$ and $_{p}\mathcal{I}$ local problems to solve.

Hence, the boundary conditions resumed in Table 3 are directly implemented in ANSYS for each local problem. The symmetry mirror used to define the eighth unit cell is taken as ANSYS boundary planes of symmetry. The null conditions listed in Table 3 are not necessary to specify because they are the default conditions. Then, for each local problem, the no-null conditions must be set up. For example:
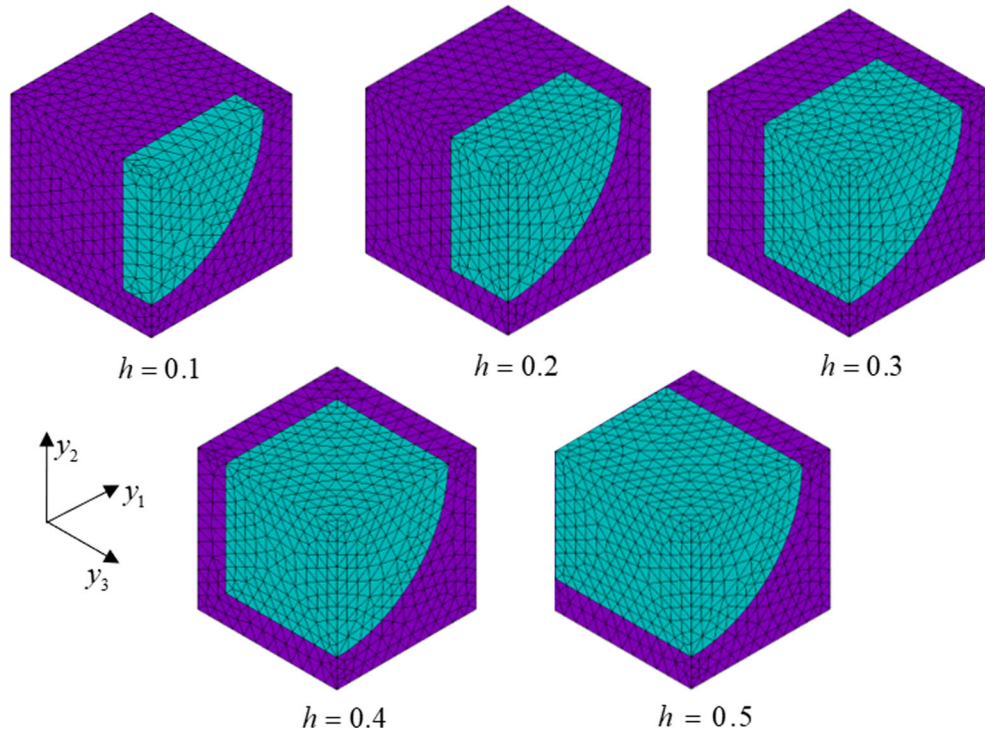
Fig. 3 Finite element mesh for one-eighth of the periodic unit cell with different relative fiber lengths

For the $_{11}\mathcal{L}$ problem, $_{11}\hat{L}_1 = d_1$ in $\{y_1 = d_h,\ y_2,\ y_3\}$, or, for the local $_1\mathcal{I}$ problem, $_1\hat{Q} = y_1$ in $\{y_1 = d_h,\ y_2,\ y_3\}$.

At this point, all is set to run the program. Once, the solution is done, the final step is to calculate the effective properties [Eqs. (21) and (22)]. The volume average values require for these equations can be calculated by ANSYS using the Element table option.

3 Analysis of results

A herein 3D SAFEM model for estimating the effective piezoelectric behavior can be useful in the design and optimization of a variety of devices, as well as to permit more realistic analysis in the biomechanics field. In Sect. 3.1, the analysis of a short-fiber-reinforced composite shows how piezoelectric properties can be manipulated taking advantages of the possibilities offered by a 3D structure. Therefore, in Sect. 3.2, the herein developed 3D SAFEM model is applied to contribute to the understanding of the bone piezoelectric behavior and to better address the key issues that need to be investigated.

3.1 Short piezoelectric fiber

The numerical simulations were conducted for different cases of 3D two-phase short FRC (fiber/matrix) by SAFEM. Herein, composites with square and hexagonal spatial fiber distributions are considered, as can be seen in Figs. 1 and 2. Besides, the effect of fiber length on the effective piezoelectric properties is analyzed under a constant fiber volume fraction or constant fiber radius. For calculations, the elastic, piezoelectric, and dielectric properties of constituent materials for fibers (PZT-5) and matrix (epoxy polymer) are taken from Ref. [18] and reported in Table 4.

Six elastic C_{1111}^*, C_{1122}^*, C_{1133}^*, C_{3333}^*, C_{1313}^* and C_{1212}^*, three piezoelectric e_{311}^*, e_{113}^* and e_{333}^*, and two dielectric κ_{11}^* and κ_{33}^*, effective coefficients are calculated using SAFEM numerical implementation. It can be noticed that the composite effective properties have a tetragonal class symmetry, which is different from the constituent's symmetry group. The SAFEM numerical results are compared with results obtained by AHM

Table 4 Elastic, piezoelectric, and dielectric properties for the constituent materials with $C_{1212} = (C_{1111} - C_{1122})/2$

Constituent Materials	Elastic (GPa)					Piezoelectric (C/m^2)			Dielectric (nF/m)	
	C_{1111}	C_{1122}	C_{1133}	C_{3333}	C_{1313}	e_{113}	e_{133}	e_{333}	κ_{11}	κ_{33}
PZT-5	121	75.4	75.2	111	21.1	12.3	−5.4	15.8	8.11	7.35
Epoxy	3.86	2.57	2.57	3.86	0.64	0	0	0	0.07965	0.07965
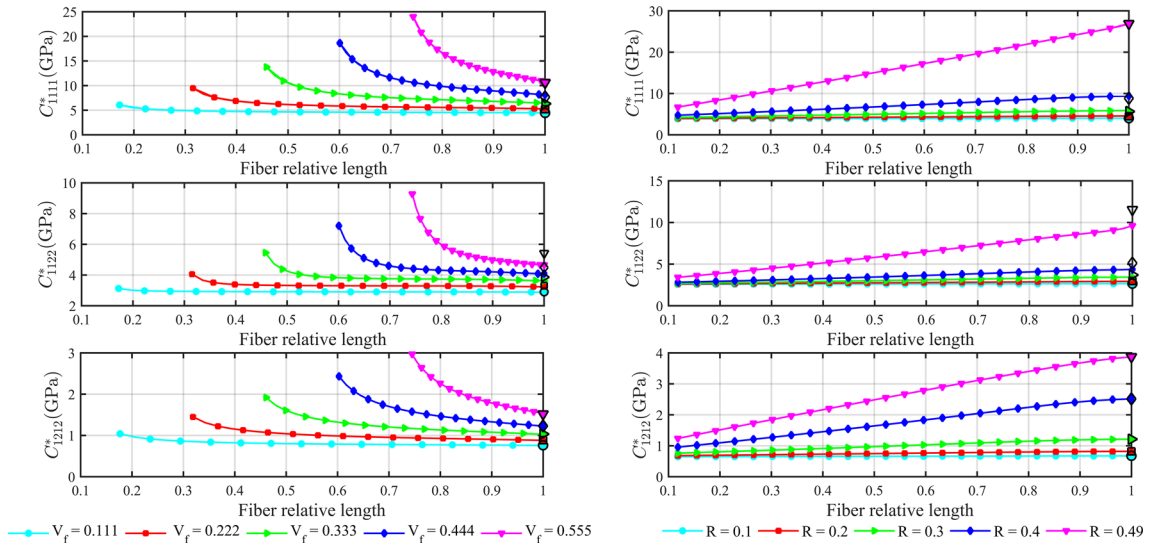
Fig. 4 Effective elastic coefficients C^*_{1111}, C^*_{1122} and C^*_{1212} of a two-phase FRC with square periodic fiber distribution cell as a function of fiber relative length for different fiber volume fractions (left) and radius (right)

with the analytical formulae of Ref. [41] and those reported by Ref. [18] using the representative volume element method (RVEM). Herein, it must be recalled that, in principle, the AHM implementation is possible for cases where a periodic heterogeneous structure is identified. FRC in the direction of long fibers is not a heterogeneous structure. On the other side, short and x_3-oriented FRC is a 3D periodic structure. As the fiber length increases, a long fiber is obtained as a limit case. Comparisons between SAFEM and the AHM analytical solution [41] are only possible for this limit case, i.e., fiber relative length close to 1.0 as much as possible. More AHM details can be found in Ref. [41]. The fiber relative length (FRL) runs from 0.0 to 1.0. As FRL tends to 1.0, the short fiber tends to the long fiber.

Figures 4, 5, 6 and 7 show the effective moduli C^*_{1111}, C^*_{1122}, and C^*_{1212} (Fig. 4), C^*_{3333}, C^*_{1313}, and C^*_{1133} (Fig. 5), e^*_{311}, e^*_{113}, and e^*_{333} (Fig. 6), κ^*_{11} and κ^*_{33} (Fig. 7) of a two-phase FRC as a function of the fiber relative length (FRL) for different fiber volume fractions (left) and fiber radius (right) with square periodic fiber distribution cell. In all the mentioned figures, the void symbols for FRL equal to 1.0 represent the values obtained by the AHM with analytically solved local problems, for long fibers. The void symbols with the same shape of solid symbols represent the same fiber volume fraction (left) or the same fiber radius (right). The same legend is used for all the figures. It is to be expected that SAFEM numerical results for the limit case of FRL tending to "1.0" should be equal to the AHM results for long fibers along the x_3-direction. As can be observed in Figs. 4, 5, 6, and 7, these expected behaviors are obtained, as FRL tends to 1.0, the SAFEM values tend to those obtained by AHM. It should also be noted the numerical difference between C^*_{1212} and C^*_{1313}, which, together with the rest properties values, lead us to conclude that the FRC presents tetragonal symmetry.

From Fig. 4, it can be noticed that C^*_{1111}, C^*_{1122}, and C^*_{1212} properties decrease as FRL increases under a constant fiber volume fraction and increases under a constant fiber radius. This is an expected result because an increase in FRL means a decrease in the fiber radius under a constant volume fraction which leads to the above-mentioned properties decrease. On the other hand, an increase in the FRL with a constant radius implies an increase in the fiber volume fraction, and therefore, C^*_{1111}, C^*_{1122}, and C^*_{1212} increases. The shear in Ox_1x_2-plane decreases for the constant fiber volume fraction and increases for the constant fiber radius as FRL increases.
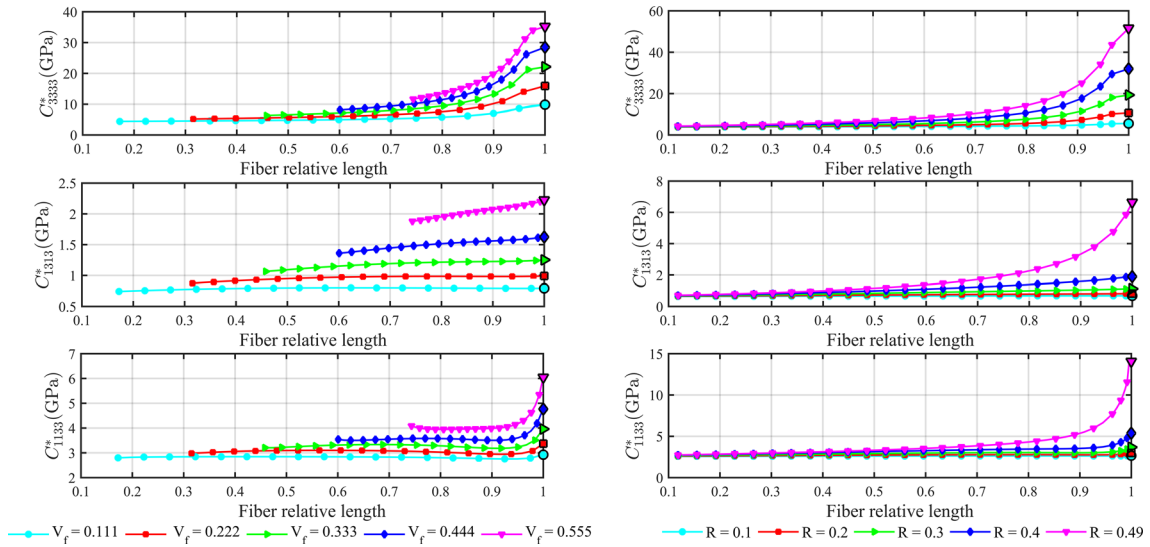
Fig. 5 Effective elastic coefficients C^*_{3333}, C^*_{1313} and C^*_{1133} of a two-phase FRC with square periodic fiber distribution cell as a function of fiber relative length for different fiber volume fractions (left) and radius (right)
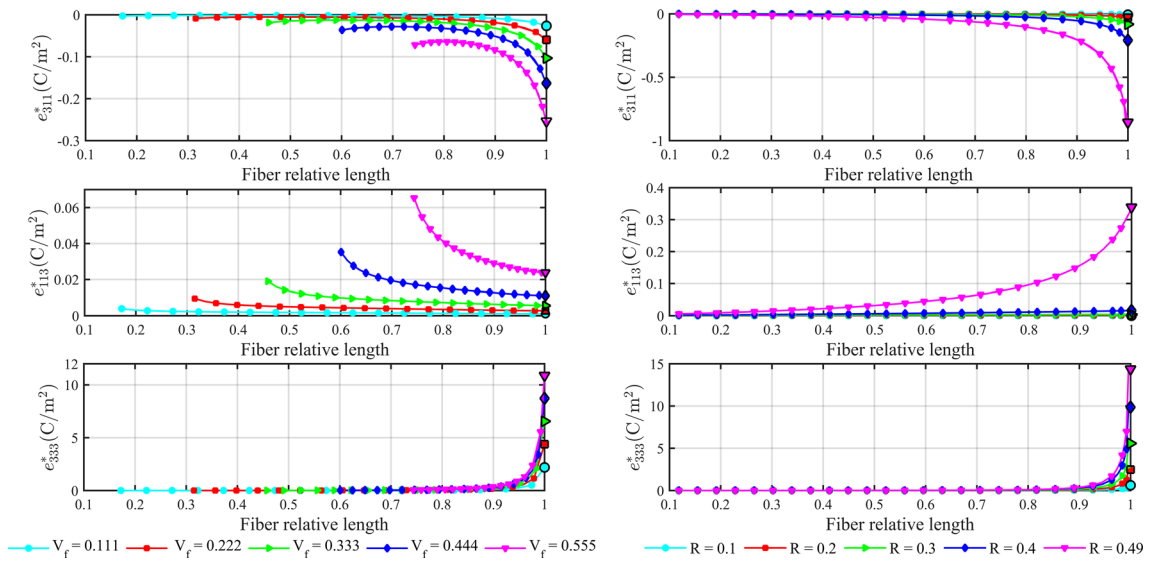

Fig. 6 Effective piezoelectric coefficients e^*_{311}, e^*_{113} and e^*_{333} of a two-phase FRC with square periodic fiber distribution cell as a function of fiber relative length for different fiber volume fractions (left) and radius (right)

In Fig. 5, it can be observed that the effective coefficient C^*_{3333}, C^*_{1313}, and C^*_{1133} increases with the FRL enlargement under both conditions: constant fiber radius and constant fiber volume fraction. A plausible explanation for the C^*_{3333} and C^*_{1133} properties behavior is due to the fact that mechanical properties along the fiber direction mainly depend on the fiber length. Let us try to understand this behavior considering the serial connection of two elastic elements. One element can be the portion of the unit cell with fiber, and the other one is the rest of the unit cell fully occupied by the matrix. For the present case, the portion with the fiber is always harder than the other one no matter what the fiber radius is. As the FRL increases, the first portion also increase always leading to an increase in the elastic effective properties C^*_{3333} and C^*_{1133}. Also, it can be observed that the shear effective coefficient C^*_{1313} increases for the two herein studied situations (constant fiber radius and constant fiber volume fraction). For these two cases, the Ox_1x_3-plane and Ox_2x_3-plane fiber axial cross section areas experiment a grow, which is the phase with higher elastic properties. For constant fiber volume (fiber radius), the axial cross section area grows directly proportional to the square root of FRL (linearly proportional to FRL). Therefore, the effective shear elasticity C^*_{1313} always increases.
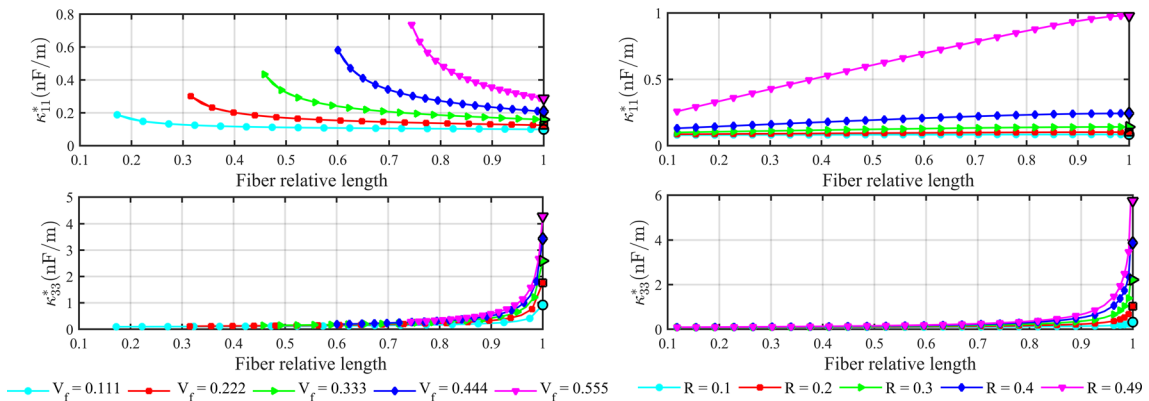
Fig. 7 Effective dielectric coefficients κ_{11}^* and κ_{33}^* of a two-phase FRC with square periodic fiber distribution cell as a function of fiber relative length for different fiber volume fractions (left) and radius (right)

Figure 6 reports the effective piezoelectric coefficients as a function of FRL for different fiber volume fractions and fiber radius. For all the cases considering constant fiber radius, the piezoelectric coefficient increases with the FRL enlargement. This is an expected result because the increase in FRL is equivalent to the increase in the piezoelectric phase volume fraction. On the other side, the constant fiber volume fraction cases imply that the piezoelectric volume fraction phase remains constant. As the FRL increases, e_{311}^* and e_{333}^* also increase. A reasonable explanation can be found in the fact that e_{311}^* and e_{333}^* connect electric and mechanical magnitudes of the x_3-direction with the x_1- and x_3-directions, respectively. Hence, the fiber x_3-direction is always involved, and we can talk again about two elements connected in series, as the FRL increase, the element volume with piezoelectric properties increases making this effect more dominant. The situation is different for e_{113}^* as this property connects magnitudes of the x_1-direction with the Ox_1x_3-plane, and the final result is the decrease in the piezoelectric property e_{311}^* with the FRL increase.

Finally, Fig. 7 shows the dependences of the dielectric effective coefficient κ_{11}^* and κ_{33}^* on the FRL. A similar behavior to the piezoelectric one can be observed. For the constant radius, the dielectric properties increase with the FRL growth. It is worthily to observe that the dielectric property κ_{33}^* slowly increases as FRL grows, but as FRL approaches to "1.0," i.e., fiber percolation, the effective properties abruptly increase. This situation is also observed for e_{333}^*, C_{3333}^*, C_{1313}^* and C_{1133}^*; and it is related to the fiber percolation, i.e., the transition from short fiber to long fiber composite. For a constant volume fraction, the dielectric property κ_{33}^* increases because it involves the component "3", on the other side, κ_{11}^* decreases as the aligned fiber x_3-direction is not directly connected with this property.

Figures 8, 9, 10 and 11 display the effective moduli C_{1111}^*, C_{1122}^* and C_{1212}^* (Fig. 8), C_{3333}^*, C_{1313}^* and C_{1133}^* (Fig. 9), e_{311}^*, e_{113}^* and e_{333}^* (Fig. 10), κ_{11}^* and κ_{33}^* (Fig. 11) of a two-phase FRC as a function of the FRL, for different fiber volume fractions (left) and fiber radius (right) with hexagonal periodic fiber distribution cell. The behavior described by these results are similar to those reports in Figs. 4, 5, 6, and 7 for square periodic fiber distribution. However, hexagonal symmetry has a higher fiber concentration which leads to higher effective properties. It is also worthily to mention that, and, for this reason, the numerical difficulties are also higher and considering this kind of fiber distribution can be seen as a contribution to the model validation.

A general comparison between the square (Figs. 4, 5, 6, 7) and hexagonal (Figs. 8, 9, 10, 11) spatial fiber distributions shows that the convergence of the short fiber SAFEM results toward the AHM analytical solution for long fiber, as the relative fiber length tends to "1.0," it is more successful for square symmetry than for hexagonal symmetry. The fiber hexagonal accommodation is more compact and near the percolation the matrix volume fraction is lower than the one of square fiber distribution. The composite matrix has to deal with higher gradient values for several physical magnitudes such as stress, strain, electric field, and electric displacements. Having the focus on the numerical quality of the results, it can be observed in Figs. 8, 9, 10, and 11, that the SAFEM predictions is good enough and trustable.

In Figs. 4, 5, 6, 7, 8, 9, 10, and 11, it can be observed a wide range of property that a short FRC permits, and it is of interest regarding possible applications. Fiber volume fraction, radius, and length offer good possibilities for property design and figures of merit can be computed with the help of a micromechanical model, like the one developed herein. Results of model implementations can be valuable for specific applications, such as piezoelectric composite transducers [46]. Further improvement in piezoelectric transducers must consider
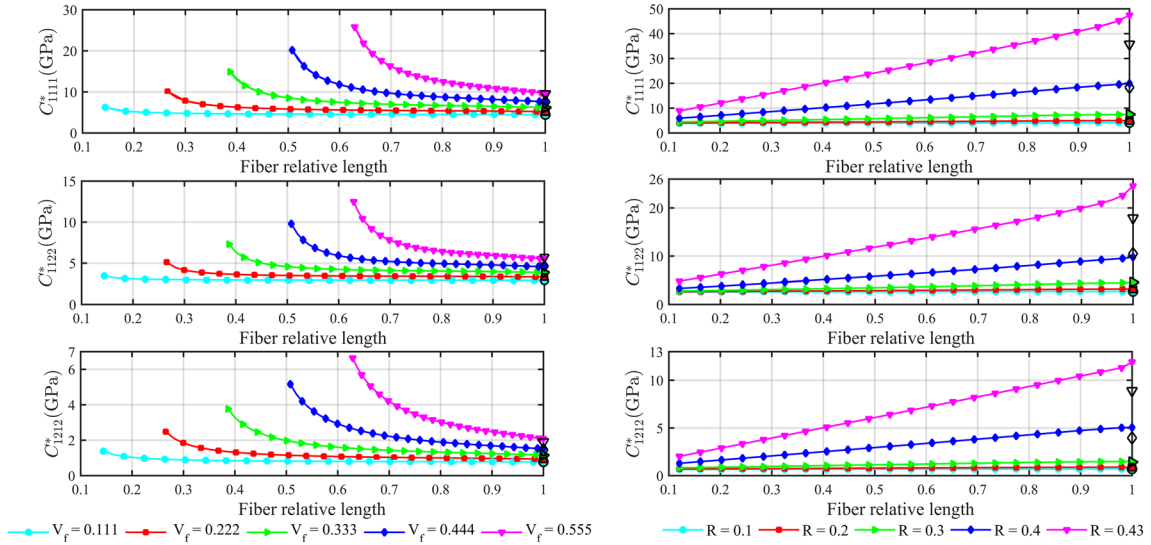
Fig. 8 Effective elastic coefficients C^*_{1111}, C^*_{1122}, and C^*_{1212} of a two-phase FRC with hexagonal periodic fiber distribution cell as a function of fiber relative length for different fiber volume fractions (left) and radius (right)
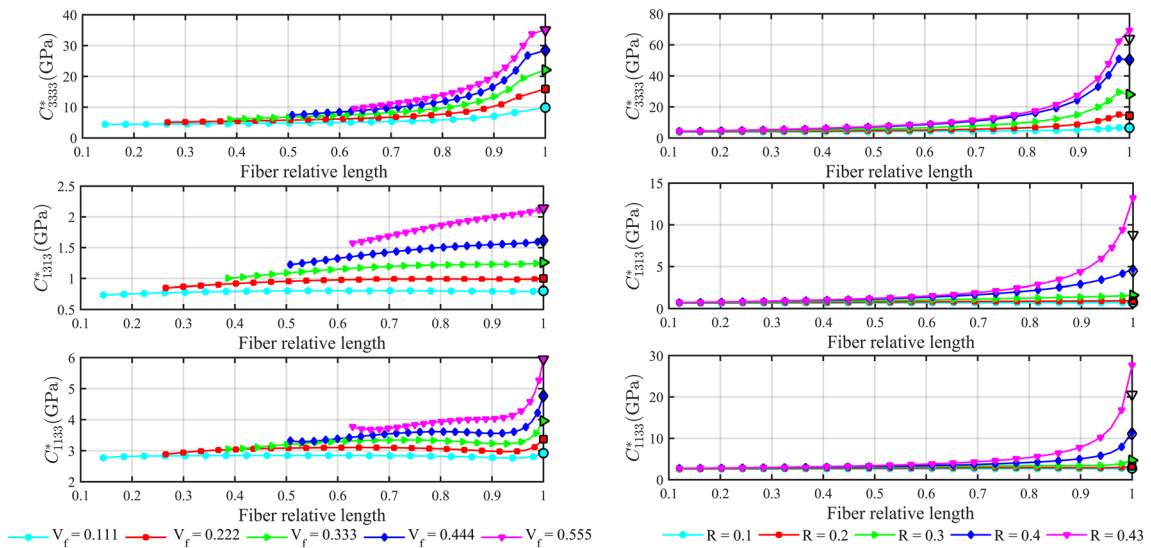

Fig. 9 Effective elastic coefficients C^*_{3333}, C^*_{1313}, and C^*_{1133} of a two-phase FRC with hexagonal periodic fiber distribution cell as a function of fiber relative length for different fiber volume fractions (left) and radius (right)

both mechanical and electrical properties, see, for instance, Gripp and Rade [47]. This kind of properties plays a key role in the electromechanical energy conversion efficiency, as can be seen in Refs. [48,49]. 3D structures are gaining space in the development of piezoelectric sensors and transducers, as it is reported in Refs. [50–52].

Tables 5 and 6 show numerical comparisons for the elastic, piezoelectric, and dielectric effective properties calculated by SAFEM herein implemented with AHM analytical solution [41] and RVEM [18] for a two-phase FRC with square fiber spatial distribution, for the limit case of the relative fiber length equal to 1.0. It can be observed that the three different models predict results very close to each other. It can be noticed that, as a general tendency, SAFEM predictions are closer to RVEM values than AHM predictions.

It can be reported that, for the numerical comparisons, the SAFEM predictions can be considered as having good quality inside of a desired range. At least two digits coincidences can always be seen comparing SAFEM with either AHM [41] or RVEM [18]. Then, the percentage error is almost always less than 3%. Three cases are worthily to mention because of high relative errors. For C^*_{1111}, and C^*_{1122} with fiber volume fraction equal to 0.667, the relative error comparing with AHM is relatively high and equal to 18.75% and 22.19%, respectively.
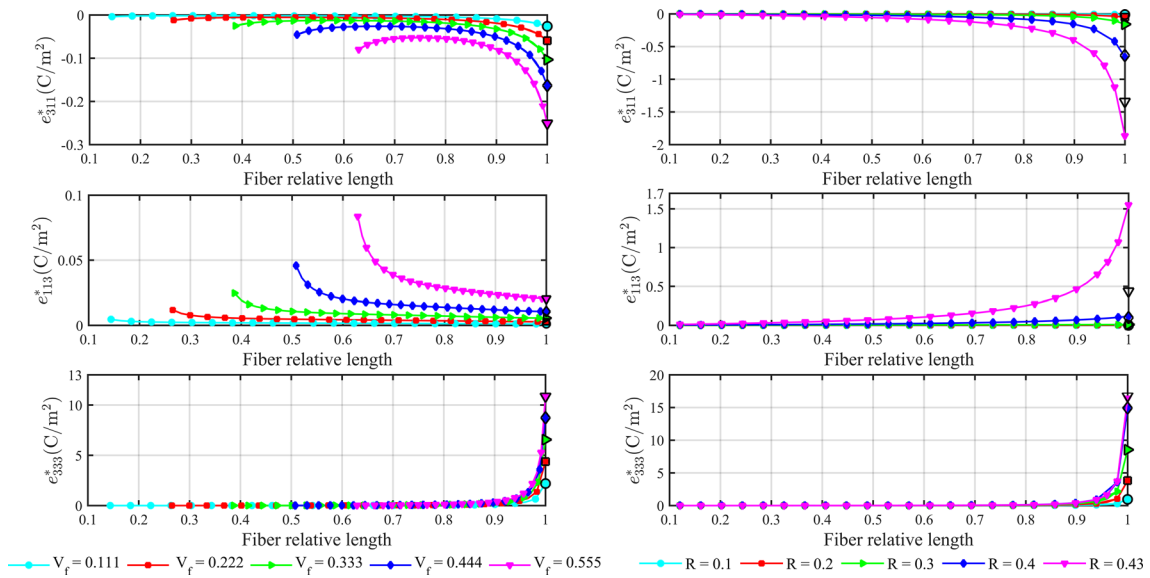
Fig. 10 Effective piezoelectric coefficients e^*_{311}, e^*_{113}, and e^*_{333} of a two-phase FRC with hexagonal periodic fiber distribution cell as a function of fiber relative length for different fiber volume fractions (left) and radius (right)
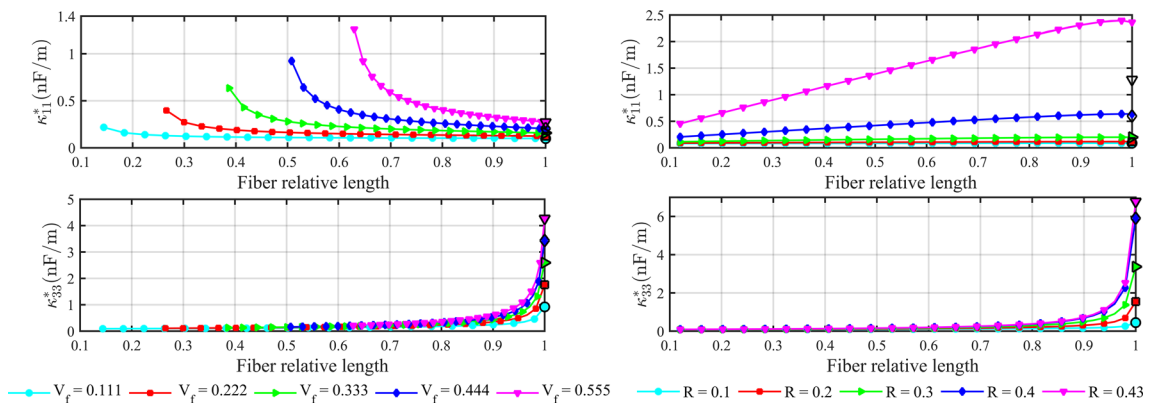

Fig. 11 Effective dielectric coefficients κ^*_{11} and κ^*_{33} of a two-phase FRC with hexagonal periodic cell as a function of fiber relative length for different fiber volume fractions (left) and radius (right)

However, the relative error comparing with RVEM is quite low and equal to 2.06% and 0.5%, respectively. The third case is the relative errors of e^*_{113} for fiber volume fraction equal to 0.556 which has the values of 0.93% for comparison with AHM and 72.98% for RVEM. Hence, the SAFEM numbers are always close to, at least, one of the two methods taken as reference for comparisons. Numerical precision is always an issue even for numerical implementation of analytical formulae. It is to be expected limitations in this sense for all approximations herein considered.

The monotone behavior for the constant fiber radius can be predicted with the Voigt–Reuss–Hill (VRH) average. The advantage of SAFEM lies in the fact that the constituent interaction is considered, then properties estimation is more realistic. In fact, most of the dependencies for the constant radius does not follow the straight line predicted by VRH average. The difference between VRH and SAFEM becomes even more physically interesting when the constant fiber volume cases are studied. According to VRH average, each property value should remain constant with the increase in the relative fiber length because of the constant volume fraction condition, i.e., as the fiber length increases, the radius decreases in such a way that the volume fraction remains constant. It must be noticed that the interaction area between phases decreases with fiber length inside the working range of Figs. 4, 5, 6, 7, 8, 9, 10, and 11. As it is reported herein, property values change according to SAFEM. For some properties, the values increase, for other ones, the values decrease with the increase in

Table 5 Comparison of the SAFEM effective elastic properties with the AHM [41] and RVEM [18] solutions for a two-phase FRC with square fiber spatial distribution

FVF	C^*_{1111} (GPa)			C^*_{1122} (GPa)			C^*_{1133} (GPa)		
	SAFEM	AHM	RVEM	SAFEM	AHM	RVEM	SAFEM	AHM	RVEM
0.111	4.4688	4.4516	4.4651	2.8826	2.9002	2.8773	2.9223	2.9224	2.9261
0.222	5.2893	5.2042	5.2558	3.2340	3.3193	3.2301	3.3703	3.3706	3.3700
0.333	6.4382	6.1985	6.4418	3.6298	3.8644	3.6244	3.9609	3.9613	3.9548
0.444	8.1333	7.5820	8.1395	4.0846	4.5934	4.0751	4.7829	4.7832	4.7750
0.556	10.922	9.6729	10.930	4.6795	5.6174	4.6572	6.0610	6.0604	6.0548
0.667	16.149	13.121	16.139	5.8230	7.1149	5.7907	8.5091	8.5048	8.5097
FVF	C^*_{3333} (GPa)			C^*_{1313} (GPa)			C^*_{1212} (GPa)		
	SAFEM	AHM	RVEM	SAFEM	AHM	RVEM	SAFEM	AHM	RVEM
0.111	9.8573	9.8575	9.5794	0.7942	0.7941	0.7919	0.7563	0.7620	0.7498
0.222	15.928	15.928	16.004	0.9907	0.9904	0.9532	0.8807	0.8872	0.8800
0.333	22.108	22.108	21.963	1.2521	1.2521	1.1934	1.0288	1.0349	1.0196
0.444	28.464	28.464	28.388	1.6240	1.6239	1.5722	1.2277	1.2290	1.2248
0.556	35.230	35.142	35.164	2.2361	2.2261	1.9123	1.5439	2.0278	1.5428
0.667	42.822	42.316	42.757	3.4491	3.4485	2.5159	2.1887	3.0029	2.1236

Table 6 Comparison of the SAFEM effective piezoelectric and dielectric properties with the AHM [41] and RVEM [18] solutions for a two-phase FRC with square fiber spatial distribution

FVF	$-e^*_{311}$ (C/m^2)			e^*_{113} (C/m^2)			e^*_{333} (C/m^2)		
	SAFEM	AHM	RVEM	SAFEM	AHM	RVEM	SAFEM	AHM	RVEM
0.111	0.0262	0.0262	0.0261	0.0011	0.0011	0.0011	2.1921	2.1921	2.1956
0.222	0.0595	0.0595	0.0604	0.0028	0.0028	0.0026	4.3788	4.3788	4.3735
0.333	0.1034	0.1033	0.1031	0.0057	0.0057	0.0052	6.5573	6.5574	6.5515
0.444	0.1645	0.1633	0.1647	0.0111	0.0111	0.0096	8.7227	8.7236	8.7119
0.556	0.2597	0.2519	0.2594	0.0107	0.0108	0.0185	10.883	10.888	10.890
0.667	0.4416	0.3924	0.4407	0.0309	0.0306	0.0439	12.956	12.993	12.963
FVF	κ^*_{11} (nF/m)			κ^*_{33} (nF/m)					
	SAFEM	AHM	RVEM	SAFEM		AHM	RVEM		
0.111	0.09931	0.09908	0.10095	0.91924		0.91925	0.86729		
0.222	0.12453	0.12391	0.12470	1.75844		1.75844	1.75592		
0.333	0.15835	0.15713	0.15677	2.59703		2.59703	2.57346		
0.444	0.20703	0.20460	0.20546	3.43464		3.43464	3.39098		
0.556	0.28704	0.28196	0.28741	4.27701		4.25575	4.27251		
0.667	0.44183	0.44140	0.44893	5.10833		5.09092	5.10427		

FRL. Therefore, it cannot be established a universal relation connecting the interphase area with the monotonic behavior of the elastic, piezoelectric, or dielectric properties.

The explanation of this behavior can be found in the constituent interaction that can be described by SAFEM as it includes the governing equations for the mechanical equilibrium and the Gauss electric field divergence. As explained above, SAFEM is based on AHM where asymptotic expansions [Eqs. (5) and (6)] are proposed for each physical variable starting from Eqs. (7) and (8). Similar expansions are part of the SAFEM implementation for the mechanical stresses and strains, as well as the electric field and the electric displacements. For all cases, the term of null order of the asymptotic expansion is defined as the pseudo-magnitude [Eqs. (5) and (6)], for example, pseudo-stress and pseudo-electric field displacement. They are a good approximation to analyze the just mentioned physical magnitudes.

The effective elastic property C^*_{1133} is calculated as:

$$C^*_{1133} = 8 \langle _{33}\hat{\sigma}_{11} \rangle, \tag{23}$$

According to Eq. (23), the effective elastic property C^*_{1133} describes the stress response σ_{11} along the x_1-direction due to an imposed displacement in the x_3-direction: u_3 (see Table 3 for the local problem $_{33}\mathcal{L}$).
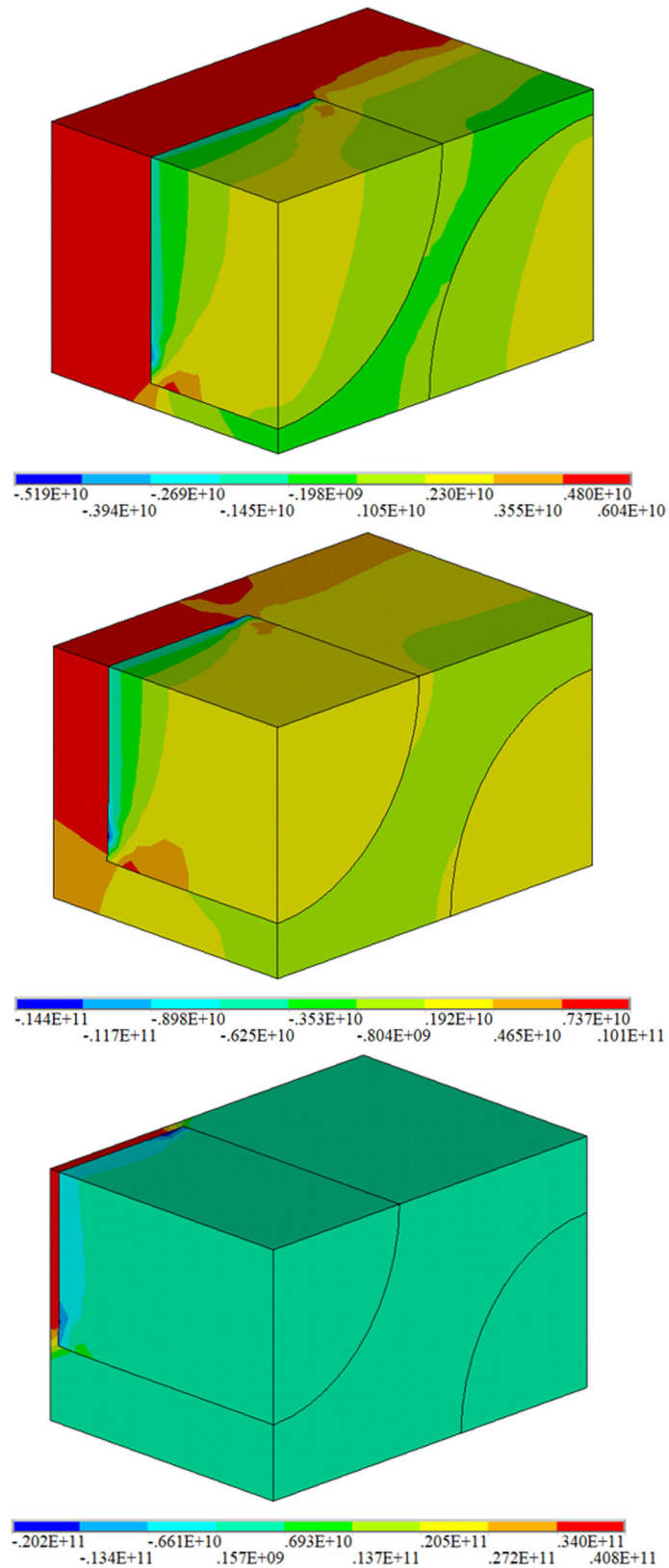
Fig. 12 The σ_{11} pseudo-stress field for the relative fiber length equal to 0.3 (upper), 0.4 (middle) and 0.49 (lower) according to Local problem $_{33}\mathcal{L}$. Fiber is along y_3-direction as seen in Fig. 3

The stress σ_{11}, which is perpendicular to the fiber direction, increases as the fiber length does. From Fig. 12, it can be observed that cross section perpendicular x_1-direction occupied by the ceramic fiber increases with the fiber length. Therefore, the higher presence of a harder material on this cross section requires a higher stress response resulting in a higher elastic constant for the composite.

The effective elastic C^*_{1111} and piezoelectric e^*_{311} properties can be calculated by the expressions:

$$C^*_{1111} = 8 \left\langle {}_{11}\hat{\sigma}_{11} \right\rangle, \tag{24}$$

$$e^*_{311} = 8 \left\langle {}_{11}\hat{D}_3 \right\rangle. \tag{25}$$

Figure 13 shows the D_3 pseudo-electric field displacement, and the σ_{11} mechanical pseudo-stress fields according to the boundary conditions stated in the local problem ${}_{11}\mathcal{L}$ (see Table 3). For lower relative fiber length, fiber is closer to each other, this causes a high concentration of stress in the matrix between fibers. As fiber gets longer, they get more separated which implies a lower concentration in the matrix between fibers, and hence, a decrease for the stress in the composite. The result is the decrease in C^*_{1111} as the relative fiber length increases. Regarding the displacement electric field, as expected, the higher concentration zone is located in the fiber. In this case, the fiber length increase implies a decrease in the displacement electric field, and therefore, a decrease in e^*_{311} coefficient is induced.

The effective piezoelectric e^*_{311} and dielectric κ^*_{33} properties are calculated by the expressions:

$$e^*_{311} = 8 \left\langle {}_3\hat{\sigma}_{11} \right\rangle, \tag{26}$$

$$\kappa^*_{33} = 8 \left\langle {}_3\hat{D}_3 \right\rangle. \tag{27}$$

From Fig. 14, it can be observed that the σ_{11} mechanical pseudo-stress and the D_3 pseudo-electric displacement field increase as the fiber length increases as a result of the applied electric field in the x_3-direction (see Table 3 for the local problem ${}_3\mathcal{I}$). The electric displacement increases resulting in an increase in the effective dielectric property as well. Special attention deserves the rapid increase near the full fiber length or fiber contact, it can be noticed that the representative volume of analysis can be divided into three sections according to the electric field distribution, i.e., the fiber with the highest electric field values, the matrix between fibers with the lowest electric field values and the part of the matrix with no fibers with an intermediate value for the electric field. As the fiber length increases, the section with intermediate values tends to decrease, and when this part is close to disappear, the dielectric constant in the fiber direction increases abruptly.

3.2 Bone piezoelectric behavior

Recently, the stiffening of aged bone tissue has been explained based on a micromechanical approach applied to a mineralized collagen fibril described as a fused hydroxyapatite mineral structure in a softer matrix by Penta et al. [40]. In that work, the main difference of the developed approach in comparison with previous ones lies in the fact that the authors not only consider the increase in mineral volume fraction, but also, they account for extrafibrillar mineral deposition. The result is the formation of a continuous mineral form that has been studied through an innovative multiscale framework based on 3D asymptotic homogenization. Experimental evidence of such bone structure has been reported in Refs. [40,53,54]. Tiburtius et al. [55] applied a multiscale micromechanics homogenization focused on musculoskeletal mineralized tissue (MMTs).

The herein developed 3D SAFEM approach for piezoelectric properties can be also applied to study the bone piezoelectric properties. For the calculations, we follow the scheme proposed by Penta et al. [40] where the mineralized collage fibril (MCF) and the extrafibrillar space (ES) conform the mineralized collagen fibril bundle (MCFB), which form part of the mineralized turkey leg tendon (MTLT). A complete description of this multiscale scheme can be found in Refs. [40] and [55]. Bone constituent materials are taken as hydroxyapatite (HA) P6_3 from Ref. [56] for the mineralized phase and collagen from Ref. [40]. The material constituent data is reported in Table 7. The MCFB volume fraction can be estimated to be around 80% in the MTLT according to the data reported in Refs. [57] and [58]. The fused hydroxyapatite piezoelectric properties are expected to have lower values than the crystal properties reported in Ref. [56], then, for the constituent piezoelectric properties we consider the half of the ones reported in Table 7. The finding of the exact piezoelectric properties for the fused HA in MCFB is out of the scope of the present work and, to our acknowledgment, it has not been reported yet. Further research is necessary in this area.
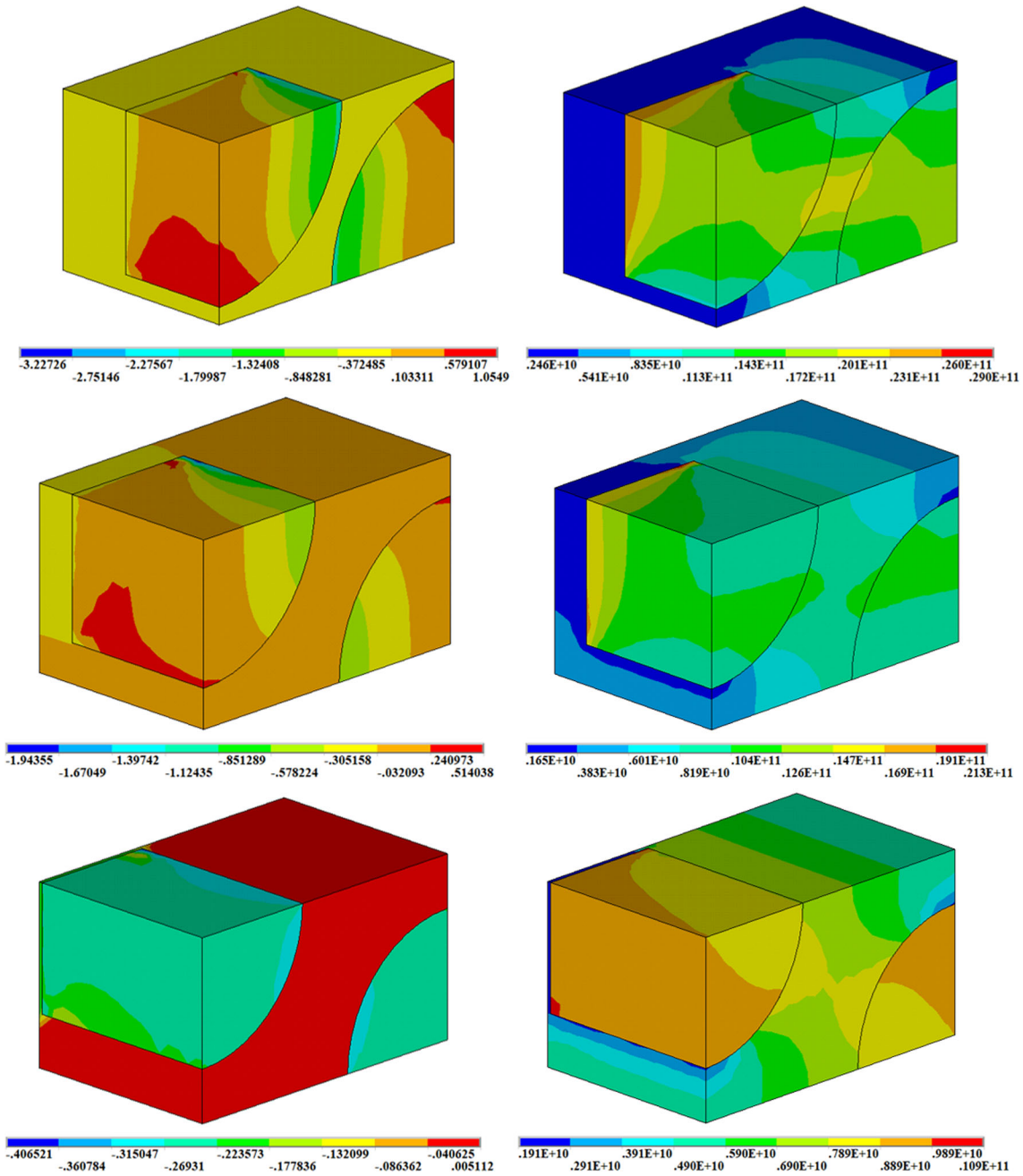
Fig. 13 The D_3 pseudo-electric field displacement (left), and σ_{11} mechanical pseudo-stress (right) for the relative fiber length equal to 0.3 (upper), 0.4 (middle) and 0.49 (lower) according to Local problem $_{11}\mathcal{L}$. Fiber is along y_3-direction as seen in Fig. 3

Table 7 Elastic, piezoelectric, and dielectric properties for bone constituent materials

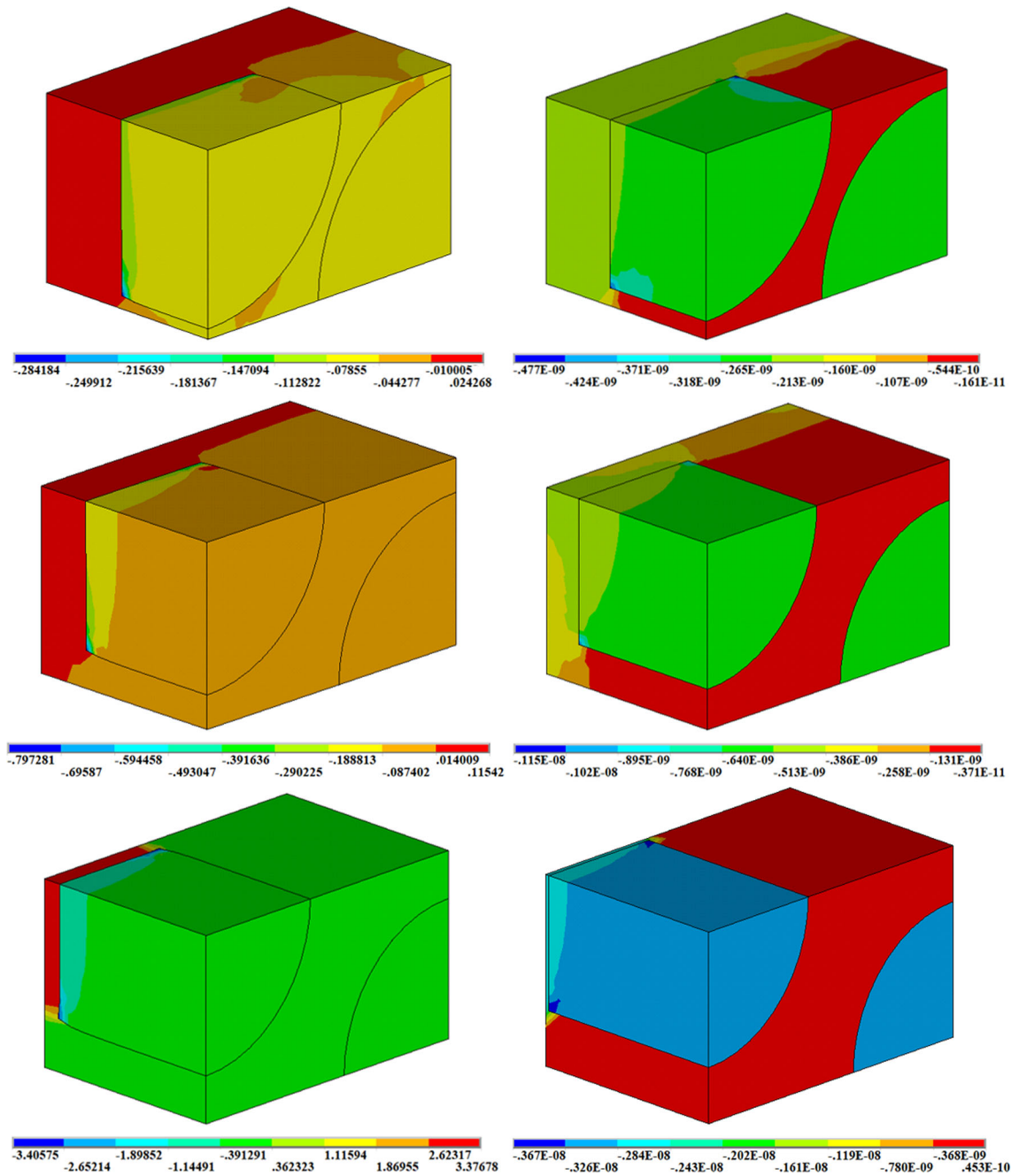| Constituent Materials	Elastic (GPa)					Piezoelectric (C/m^2)				Dielectric (nF/m)	
	C_{1111}	C_{1122}	C_{1133}	C_{3333}	C_{1313}	e_{113}	e_{133}	e_{123}	e_{333}	κ_{11}	κ_{33}
HA P6$_3$	138	45.9	69.1	172.8	51.4	0.28	2.4	-0.65	-0.47	6.446	3.914
Collagen	6.7	2.8	2.8	6.7	3.8	0.0	0.0	0.0	0.0	2.656	2.656

Fig. 14 The σ_{11} mechanical pseudo-stress (upper) and D_3 pseudo-electric displacement (lower) fields for the relative fiber length equal to 0.3 (upper), 0.4 (middle) and 0.49 (lower) according to Local problem $_3\mathcal{I}$. Fiber is along y_3-direction as seen in Fig. 3

Figure 15 illustrates the dependence of the effective C^*_{3333} elastic and d^*_{333} piezoelectric coefficients on the HA volume fraction in the MCFB. The ratio a_x/a_z is a description for the extrafibrillar mineral deposition in the MCFB where a_z and a_x are related to the fibril transverse dimension and the cross section of the bridges between fibrils, respectively. a_x/a_z less than one means that the bridges are smaller than the fibril cross section dimension (see, for instance, Fig. 7(a) in Ref. [40]). The C^*_{3333} effective values are quite similar to those reported by Penta et al. [40] and inside the range of the experimental data that run from around 20 to 80 GPa for a HA volume fraction in MCBF between 0.35 and 0.41 (see, for instance, Fig. 9(a) in Ref. [40]). Totally matching results between the present model and those reported by Penta et al. [40] are not obtained because, here, different constituent properties are considered for HA in order to consider the piezoelectric effect, as can
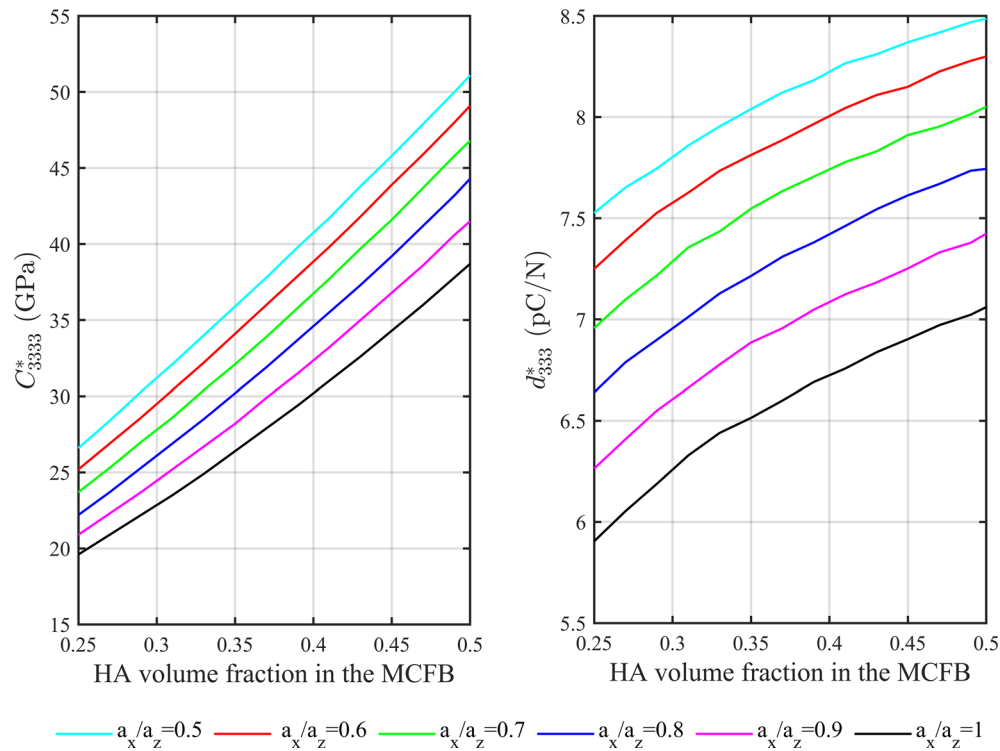
Fig. 15 Dependence of the effective C^*_{3333} elastic and d^*_{333} piezoelectric coefficient on the hydroxyapatite (HA) volume fraction in the mineralized collagen fibril bundle (MCFB)

be seen in Table 7. The d^*_{333} effective coefficient is calculated according to the relation $d^*_{333} = e^*_{3jj} S^*_{33jj}$ where $S^*_{ijkl} = (C^*_{ijkl})^{-1}$ is the effective compliance elastic matrix.

The effective piezoelectric coefficient (d^*_{333}) in Fig. 15 is obtained in the range between 7.0 and 9.0 pC/N. Halperin et al. [59] studied the bone piezoelectric coefficient with the help of piezoresponse force microscopy (PFM) and obtained values between 7.66 and 8.72 pC/N. This congruent result for the bone piezoelectric behavior is obtained under the assumption that the fused HA has lower piezoelectric properties than crystal HA. Direct experimental evidence for this consideration is not available, but the bone structure characterization reported in Refs. [54] and [53] suggest the above mentioned assumption. Lees et al. [57] and Alexander et al. [58] have shown that, at least, a crystal-oriented structure is not present. This is a key issue that needs to be addressed for better understanding the bone piezoelectric behavior where the aid of the 3D micromechanical description should be a useful tool.

4 Conclusions

A 3D semi-analytical approach (SAFEM) for piezoelectric materials to calculate composite effective properties has been stated. Validations are developed using comparisons with numerical results reported in the literature, for limit cases. SAFEM is based on the local problems derived from the asymptotic homogenization method (AHM) and solving them by finite element analysis (FEA).

Short-fiber-reinforced composites are studied as a function of the fiber relative length (FRL) that runs from nearly zero to one. As the FRL tends to one, the short fiber composite tends to the long fiber-reinforced composite. For this limit case, comparisons between the AHM and FEM show good coincidences.

The constant fiber volume fraction herein studied is of interest because according to Voigt–Reuss–Hill approximation, effective properties only depend on fiber volume fraction. Through SAFEM, phases interaction is considered because the stress equilibrium and Gauss law are included. Herein, piezoelectric effective properties are obtained as a function of the fiber volume fraction and different behaviors are observed. The increasing or decreasing behaviors of the effective properties depend on the physical magnitudes distributions that result from certain local problems developed for the properties estimations. In general, the effective

properties increments are observed for those cases where the fiber direction is involved in one of the physical magnitudes connected by the specific property; for example, C^*_{3333}, C^*_{1313}, C^*_{1133}, e^*_{311}, e^*_{333}, and κ^*_{33}. When constant fiber radius is analyzed, the monotone behavior coincides with the Voigt–Reuss–Hill averages, but with different slopes as result of phase interaction. It should be mentioned that C^*_{3333}, C^*_{1313}, C^*_{1133}, e^*_{311}, e^*_{113}, e^*_{333}, and κ^*_{33} (properties connected with the x_3-fiber direction) tends to slowly increase with the FRL increment and when the fiber percolation is close, the properties abruptly increase. In resume, the 3D structure of Short-fiber-reinforced composite offers the possibility to manipulate properties inside of a considerable range of values.

Finally, the herein developed model allows us to analyze the bone piezoelectric behavior. It must be noticed that it is possible to explain the experimental measured d^*_{333} piezoelectric coefficient if the constituent mineralized phase is considered to have piezoelectric coefficients lower than the one reported for the hydroxyapatite (HA) in the literature. It is congruent to suppose that fused HA of the mineralized phase in bone has a lower piezoelectric coefficient than the crystalline HA reported in the literature.

References

1. Cook-Chennault, K.A., Thambi, N., Sastry, A.M.: Powering MEMS portable devices—a review of non-regenerative and regenerative power supply systems with special emphasis on piezoelectric energy harvesting systems. Smart Mater. Struct. **17**, 43001 (2008)
2. Eynbeygi, M., Aghdam, M.M.: A micromechanical study on the electro-elastic behavior of piezoelectric fiber-reinforced composites using the element-free Galerkin method. Acta Mech. **226**, 3177–3194 (2015)
3. Vijaya, M.: Piezoelectric Materials and Devices. CRC Press, Boca Raton (2013)
4. Bowen, C.R., Topolov, V.Y., Kim, H.A.: Modern Piezoelectric Energy-Harvesting Materials. Springer Series in Materials Science, vol. 238. Springer, Berlin (2016)
5. Cholleti, E.R.: A review on 3D printing of piezoelectric materials. IOP Conf. Ser. Mater. Sci. Eng. **455**, 12046 (2018)
6. Newnham, R.E.: Composite electroceramics. Ferroelectrics **68**, 1–32 (1986)
7. Gururaja, T.R., Schulze, W.A., Cross, L.E., Newnham, R.E., Auld, B.A., Wang, Y.J.: Piezoelectric composite materials for ultrasonic transducer applications. Part I: resonant modes of vibration of PZT rod-polymer composites. IEEE Trans. Sonics Ultrasonics **32**, 481–498 (1985)
8. Rödel, J., Jo, W., Seifert, K.T.P., Anton, E.-M., Granzow, T., Damjanovic, D.: Perspective on the development of lead-free piezoceramics. J. Am. Ceram. Soc. **92**, 1153–1177 (2009)
9. Gocha, A.: Smart materials make smart phones: how ceramics and glass contribute to the \$479B smartphone market. Am. Ceram. Soc. Bull. **97**, 11–23 (2018)
10. El Messiery, M.A., Hastings, G.W., Rakowski, S.: Ferro-electricity of dry cortical bone. J. Biomed. Eng. **1**, 63–65 (1979)
11. Gandhi, A.A., Wojtas, M., Lang, S.B., Kholkin, A.L., Tofail, S.A.M.: Piezoelectricity in poled hydroxyapatite ceramics. J. Am. Ceram. Soc. **97**, 2867–2872 (2014)
12. Tang, Y., Wu, C., Wu, Z., Hu, L., Zhang, W., Zhao, K.: Fabrication and in vitro biological properties of piezoelectric bioceramics for bone regeneration. Sci. Rep. **7**, 43360 (2017)
13. Jacob, J., More, N., Kalia, K., Kapusetti, G.: Piezoelectric smart biomaterials for bone and cartilage tissue engineering. Inflamm. Regen. **38**, 1–11 (2018)
14. Silva, C.C., Thomazini, D., Pinheiro, A.G., Aranha, N., Figueiró, S.D., Góes, J.C., Sombra, A.S.B.: Collagen-hydroxyapatite films: piezoelectric properties. Mater. Sci. Eng. B **86**, 210–218 (2001)
15. Miara, B., Rohan, E., Zidi, M., Labat, B.: Piezomaterials for bone regeneration design—homogenization approach. J. Mech. Phys. Solids. **53**, 2529–2556 (2005)
16. Bersani, A.M., Bersani, E., Dell'Acqua, G., Pedersen, M.G.: New trends and perspectives in nonlinear intracellular dynamics: one century from Michaelis–Menten paper. Contin. Mech. Thermodyn. **27**, 659–684 (2015)
17. Mohammadkhah, M., Marinkovic, D., Zehn, M., Checa, S.: A review on computer modeling of bone piezoelectricity and its application to bone adaptation and regeneration. Bone **127**, 544–555 (2019)
18. Berger, H., Kari, S., Gabbert, U., Rodriguez-Ramos, R., Guinovart, R., Otero, J.A., Bravo-Castillero, J.: An analytical and numerical approach for calculating effective material coefficients of piezoelectric fiber composites. Int. J. Solids Struct. **42**, 5692–5714 (2005)
19. Dunn, M.L., Taya, M.: Micromechanics predictions of the effective electroelastic moduli of piezoelectric composites. Int. J. Solids Struct. **30**, 161–175 (1993)
20. Guinovart-Díaz, R., Rodríguez-Ramos, R., Espinosa-Almeyda, Y., López-Realpozo, J.C., Dumont, S., Lebon, F., Conci, A.: An approach for modeling three-phase piezoelectric composites. Math. Methods Appl. Sci. **40**, 3230–3248 (2017)
21. Panda, S.P., Panda, S.: Micromechanical finite element analysis of effective properties of a unidirectional short piezoelectric fiber reinforced composite. Int. J. Mech. Mater. Des. **11**, 41–57 (2015)
22. Qin, R.-S., Xiao, Y., Lan, H.: Numerical simulation of effective properties of 3D piezoelectric composites. J. Eng. **2014**, 1–14 (2014)

23. Wei, E.-B., Poon, Y.M., Shin, F.G., Gu, G.Q.: Effective properties of piezoelectric composites with periodic structure. Phys. Rev. B. **74**, 14107 (2006)
24. Piccardo, G., D'Annibale, F., Zulli, D.: On the contribution of Angelo Luongo to Mechanics: in honor of his 60th birthday. Contin. Mech. Thermodyn. **27**, 507–529 (2015)
25. Zhou, Z., Ni, Y., Zhu, S., Tong, Z., Sun, J., Xu, X.: An accurate and straightforward approach to thermo-electro-mechanical vibration of piezoelectric fiber-reinforced composite cylindrical shells. Compos. Struct. **207**, 292–303 (2019)
26. Hasanzadeh, M., Ansari, R., Hassanzadeh-Aghdam, M.K.: Evaluation of effective properties of piezoelectric hybrid composites containing carbon nanotubes. Mech. Mater. **129**, 63–79 (2019)
27. Xu, Y., Xiao, J., Jia, J., Qiu, P., Zhao, Q.: An analytical method for piezoelectric composites containing doubly periodic piezoelectric fibers with ring-shaped cross-section under antiplane shear and its application. Comput. Mater. Sci. **88**, 7–13 (2014)
28. Ma, X., Wei, G.: Numerical prediction of effective electro-elastic properties of three-dimensional braided piezoelectric ceramic composites. Compos. Struct. **180**, 420–428 (2017)
29. Lee, J., Boyd, J.G., Lagoudas, D.C.: Effective properties of three-phase electro-magneto-elastic composites. Int. J. Eng. Sci. **43**, 790–825 (2005)
30. McCartney, L.N., Crocker, L.E., Wright, L.: Verification of a 3D analytical model of multilayered piezoelectric systems using finite element analysis. J. Appl. Phys. **125**, 184503 (2019)
31. Zhang, J., Eisenträger, J., Duczek, S., Song, C.: Discrete modeling of fiber reinforced composites using the scaled boundary finite element method. Compos. Struct. **235**, 111744 (2020)
32. Dubey, M.K., Panda, S.: Electromechanical properties and actuation capability of an extension mode piezoelectric fiber composite actuator with cylindrically periodic microstructure. Arch. Appl. Mech. **88**, 2261–2281 (2018)
33. Sreenivasa Prasath, S., Arockiarajan, A.: Analytical, numerical and experimental predictions of the effective electromechanical properties of macro-fiber composite (MFC). Sens. Actuators A Phys. **214**, 31–44 (2014)
34. Otero, J.A., Rodríguez-Ramos, R., Bravo-Castillero, J., Guinovart-Díaz, R., Sabina, F.J., Monsivais, G.: Semi-analytical method for computing effective properties in elastic composite under imperfect contact. Int. J. Solids Struct. **50**, 609–622 (2013)
35. Otero, J.A., Rodríguez-Ramos, R., Monsivais, G.: Computation of effective properties in elastic composites under imperfect contact with different inclusion shapes. Math. Methods Appl. Sci. **40**, 3290–3310 (2017)
36. Bakhvalov, N.S., Panasenko, G.P.: Homogenization Averaging Processes in Periodic Media. Kluwer Academic, Dordrecht (1989)
37. Pobedrya, B.E.: Mechanics of Composite Materials. Moscow State University Press, Moscow (1984).. (**(in Russian)**)
38. Breuer, K., Stommel, M.: RVE modelling of short fiber reinforced thermoplastics with discrete fiber orientation and fiber length distribution. SN Appl. Sci. **2**, 91 (2020)
39. Chen, L., Gu, B., Zhou, J., Tao, J.: Study of the effectiveness of the RVEs for random short fiber reinforced elastomer composites. Fibers Polym. **20**, 1467–1479 (2019)
40. Penta, R., Raum, K., Grimal, Q., Schrof, S., Gerisch, A.: Can a continuous mineral foam explain the stiffening of aged bone tissue? A micromechanical approach to mineral fusion in musculoskeletal tissues. Bioinspir. Biomim. **11**, 35004 (2016)
41. Bravo-Castillero, J., Guinovart-Díaz, R., Sabina, F.J., Rodríguez-Ramos, R.: Closed-form expressions for the effective coefficients of a fiber-reinforced composite with transversely isotropic constituents—II. Piezoelectric and square symmetry. Mech. Mater. **33**, 237–248 (2001)
42. Sánchez-Palencia, E.: Non Homogeneous Media and Vibration Theory. Springer, Berlin (1980)
43. Sabina, F.J., Rodríguez-Ramos, R., Bravo-Castillero, J., Guinovart-Díaz, R.: Closed-form expressions for the effective coefficients of a fibre-reinforced composite with transversely isotropic constituents. II: Piezoelectric and hexagonal symmetry. J. Mech. Phys. Solids. **49**, 1463–1479 (2001)
44. Rodríguez-Ramos, R., Sabina, F.J., Guinovart-Díaz, R., Bravo-Castillero, J.: Closed-form expressions for the effective coefficients of a fiber-reinforced composite with transversely isotropic constituents—I. Elastic and square symmetry. Mech. Mater. **33**, 223–235 (2001)
45. Rodríguez-Ramos, R., de Medeiros, R., Guinovart-Díaz, R., Bravo-Castillero, J., Otero, J.A., Tita, V.: Different approaches for calculating the effective elastic properties in composite materials under imperfect contact adherence. Compos. Struct. **99**, 264–275 (2013)
46. Lee, H.J., Zhang, S., Bar-Cohen, Y., Sherrit, S.: High temperature, high power piezoelectric composite transducers. Sensors **14**, 14526–14552 (2014)
47. Gripp, J.A.B., Rade, D.A.: Vibration and noise control using shunted piezoelectric transducers: a review. Mech. Syst. Signal Process. **112**, 359–383 (2018)
48. Cao, Y., Sha, A., Liu, Z., Li, J., Jiang, W.: Energy output of piezoelectric transducers and pavements under simulated traffic load. J. Clean. Prod. **279**, 123508 (2021)
49. Pan, C.-T., Wang, S.-Y., Yen, C.-K., Kumar, A., Kuo, S.-W., Zheng, J.-L., Wen, Z.-H., Singh, R., Singh, S.P., Khan, M.T., Chaudhary, R.K., Dai, X., Chandra Kaushik, A., Wei, D.-Q., Shiue, Y.-L., Chang, W.-H.: Polyvinylidene fluoride-added ceramic powder composite near-field electrospinned piezoelectric fiber-based low-frequency dynamic sensors. ACS Omega **5**, 17090–17101 (2020)
50. Ma, G., Li, Y., Wang, L., Zhang, J., Li, Z.: Real-time quantification of fresh and hardened mechanical property for 3D printing material by intellectualization with piezoelectric transducers. Constr. Build. Mater. **241**, 117982 (2020)
51. Omoniyi, O.A., Mansour, R., Reid, A., Liang, L., O'Leary, R., Windmill, J.F.C.: 3D-printing of a piezocomposite material with high filler content for transducer applications. In: 2020 IEEE International Ultrasonics Symposium (IUS), pp. 1–3 (2020)
52. Assagra, Y.A.O., Altafim, R.A.P., do Carmo, J.P., Altafim, R.A.C., Rychkov, D., Wirges, W., Gerhard, R.: A new route to piezo-polymer transducers: 3D printing of polypropylene ferroelectrets. IEEE Trans. Dielectr. Electr. Insul. **27**, 1668–1674 (2020)

53. Rosen, V.B., Hobbs, L.W., Spector, M.: The ultrastructure of anorganic bovine bone and selected synthetic hyroxyapatites used as bone graft substitute materials. Biomaterials **23**, 921–928 (2002)
54. Chen, P.-Y., Toroian, D., Price, P.A., McKittrick, J.: Minerals form a continuum phase in mature cancellous bone. Calcif. Tissue Int. **88**, 351–361 (2011)
55. Tiburtius, S., Schrof, S., Molnár, F., Varga, P., Peyrin, F., Grimal, Q., Raum, K., Gerisch, A.: On the elastic properties of mineralized turkey leg tendon tissue: multiscale model and experiment. Biomech. Model. Mechanobiol. **13**, 1003–1023 (2014)
56. Tofail, S.A.M., Haverty, D., Stanton, K.T., McMonagle, J.B.: Structural order and dielectric behaviour of hydroxyapatite. Ferroelectrics. **319**, 117–123 (2005)
57. Lees, S., Prostak, K.S., Ingle, V.K., Kjoller, K.: The loci of mineral in turkey leg tendon as seen by atomic force microscope and electron microscopy. Calcif. Tissue Int. **55**, 180–189 (1994)
58. Alexander, B., Daulton, T.L., Genin, G.M., Lipner, J., Pasteris, J.D., Wopenka, B., Thomopoulos, S.: The nanometre-scale physiology of bone: steric modelling and scanning transmission electron microscopy of collagen-mineral structure. J. R. Soc. Interface. **9**, 1774–1786 (2012)
59. Halperin, C., Mutchnik, S., Agronin, A., Molotskii, M., Urenski, P., Salai, M., Rosenman, G.: Piezoelectric effect in human bones studied in nanometer scale. Nano Lett. **4**, 1253–1256 (2004)